03

Daewoo Construction Technology Report



플랜트/환경

- Performance evaluation of two-stage spiral wound forward osmosis elements at various operation conditions
- O_3/BAC 공정에서 후단여과막 적용성 연구
- Analytical and numerical assessments of local overpressure from hydrogen gas explosions in petrochemical plants
- Method for Installation of Marine HDPE Pipeline



Performance evaluation of two-stage spiral wound forward osmosis elements at various operation conditions

Sung-Ju Im
Graduate School of Water Resources, Sungkyunkwan University
juim90@gmail.com

Gi-Ho Park
Civil & Plant Engineering Research Team, DICT
giho.park@daewooenc.com

Gyeong-Wan Go
Graduate School of Water Resources, Sungkyunkwan University
ogyeongwan8329@gmail.com

Am Jang
Graduate School of Water Resources, Sungkyunkwan University
amjang@skku.edu

Sang-Hak Lee
Huviswater Corporation
leesh@huviswater.com

본 논문은 2016년 Desalination and Water Treatment Vol.57, 2016, pp. 24583-24594에 게재되었던 논문을 재게재한 것입니다.

Abstract

정삼투 (FO)는 폐수 처리, 수자원 재사용 및 담수화를위한 물 산업에서 새롭게 부상하는 공정이다. 많은 실험실 규모의 연구가 수행되었지만 생성된 데이터는 서로다른 멤브레인 구성요소로인해 실제 파일럿 플랜트에 직접 적용될 수 없다. 본 연구에서는 다양한 운전 조건 (유도 용액 농도, 유속 및 배열 형태)에서 상업용 와권형 정삼투(SWFO) 막의 성능을 평가하였다. 먼저, 우리는 SWFO 특수 구조 (유도용액 흐름 경로의 구성)를 조사했으며 SWFO의 구조적 특성으로 인해, 유입 유속이 빠르기 때문에 유도용액의 유량은 고압 강하 효과를 나타냈다. 두 번째로는 서로 다른 요소 배열 유형의 성능을 연구하였다. 양측의 유속 변화는 농도 분극 및 희석 효과를 줄임으로써 pilot-scale SWFO의 성능에 영향을 미쳤다. 또한, SWFO 요소 배열의 유형에 따라 유속은 물 플럭스에서 다른 역할을 보였다. 우리는 파일럿 플랜트에 직접 적용 가능한 요소 평가를 수행하기위해 상용 FO 공정의 설계 및 관리 지침을 제안하였고 이 연구는 FO 공정 분야의 엔지니어에게 중요한 참고 자료로 사용될 수 있을 것이다.

Keywords : Forward osmosis; Pilot-scale; Spiral wound element; Flow rate; Water flux

1_INTRODUCTION

To overcome or attenuate global warming and water scarcity crises, enormous efforts and research studies have been done to identify novel methods to purify wastewater or seawater at low cost with low energy consumption [1–3].Membrane process such as reverse osmosis (RO), nanofiltration (NF), and ultrafiltration (UF) have emerged for water treatment, desalination, and water reuse because the area for membrane process installation is compact. In addition, their removal efficiency is higher than traditional water treatment processes such as sand filtration or settling reservoir [2–4].

RO and NF are effective and commercially available technologies in the water industry [4,5]. However, pressure-driven membrane processes require expensive capital expenditures (CAPEX) and operating expenditures (OPEX) because they necessitate high hydraulic pressure to overcome the source osmotic pressure with resistance to foulants [2,6,7]. Forward osmosis (FO) is one mem-

brane process driven by different mechanisms. In the FO process, water is transported through semi-permeable membrane from a low concentration solution (feed solution) to a high concentration solution (draw solution) creating a difference in osmotic pressure [8]. The basic FO mechanism has many advantages such as high water recovery, low operation pressure, less fouling tendency, and easy cleaning. For these reasons, FO is widely used in food, medical, and pharmaceutical industries except for water treatment [8–11]. In order to influence the water industry, FO must prove to surpass the current water purification processes. First, the FO membrane needs to have high water permeation with superior salt separation. Second, the FO process should reach similar theoretical value. Third, FO researchers need to find a suitable draw solution and fouling control for FO management. Fourth, the FO process needs to address problems such as concentration polarization (CP), cleaning methods, membrane lifetime, and reverse solute flux [6,12–14]. Many FO membrane and process studies have been conducted at lab-scale level using a flat sheet membrane coupon [10,15]. A few studies used a spiral-wound membrane, however, we still need further study at the pilot-scale [11,16–18]. Nevertheless, lab-scale FO test data cannot be directly applied to a real pilot plant for water purification. Thus, after commercialized FO element evaluation, it is preferable to progress to the next step to scale up the FO process. For the evaluation of commercialized FO elements, the following need to be considered: (1) there are a few FO membrane manufacturers, such as Hydration Technology Innovations (HTI), Porifera, and Toray. (The HTI spiral wound forward osmosis (SWFO) element was used in this study); (2) spiral-wound and flat sheet elements have different configurations and flow path distance, meaning that different drops in pressure and permeate flux may develop depending on structural characteristics [15,19]. Therefore, we etermined the spiral-wound structural characteristic of SWFO through a pilot-scale apparatus. In addition, we performed comparative studies to identify capacities of two types of array (series and parallel) at various draw solution concentrations (25,000–70,000 ppm). We also examined the effect of flow rate change on FO performance. The aim of this study was to obtain directly applicable data for real pilot plant to provide basic information to scaling up the FO process.

2_MATERIALS AND METHODS

2.1. SWFO element and membrane

The commercially available SWFO element (HTI OsMem™ 2521 FO-CTA-MS-P-3H) was provided by HTI (Albany, USA) to evaluate SWFO performance. The SWFO element was made by wrapping one flat sheet membrane with embedded support. The membrane consisted of a cellulose triacetate (CTA) layer with an embedded polyester mesh for mechanical support. It is 50 μm thick [13,20]. The effective membrane area is 0.5 m^2. The lengthand width oftheelement was 0.52 and 0.48m, respectively. The SWFO element has as tand arddiamond - type feed spacer with thick nessof1. 1mm and a 3Hd rawsolution spacer1. 5mm thick. The spacer enhanced the turbulence in flow. It can reduce the CP and the rate ofmass trans feron the surfaceof membrane [15,17,21]. The SWFO element used in this study had a cross flow pattern.

The membrane active layer faced the feed solution while support layer later faced the draw solution (AL-facing-FS mode). According to its specification information, the element was capable of enduring a maximum operating temperature of 43˚C with maximum side-port pressure of five bars. The maximum transmembrane pressure (side-port exit pressure minus end-port feed pressure) was 0.35 bar. The maximum end-port inlet and outlet pressures were one bar and 0.15 bar, respectively. The solution pH ranged from 3 to 8, with maximum NTU of 10. The maximum tolerable hydraulic pressure of the polyvinyl chloride (PVC) vessel was 15 bars.

The SWFO element is different from a RO vessel because FO has different mechanisms compared to RO [2,3]. As shown in Fig. 1, the SWFO element was housed in a pressure vessel (AXEON water technologies, CA) of PVC with four ports. Two ports were for inlet of feed and draw solution. The remaining two ports were for outlet of concentrated feed and diluted draw solution.

2.2. Pilot-scale spiral-wound forward osmosis design

Fig. 2a shows a schematic diagram of the FO–RO hybrid pilot

system. Our pilot system is composed of two SWFO elements and one SWRO element. In this study, we focused on the two SWFO elements system because the SWFO evaluation must precede the operation of the FO–RO hybrid system. SWFO elements were connected in series or in parallel, in two-stage or one-stage modes. As seen in Fig. 2b, in the one-stage mode, both draw solution and feed solution flowed in each side inlet and flowed out through each side outlet. Both solutions were then fed back to each tank. In contrast, in the two-stage mode, the effluent of first FO element moved directly toward the second SWFO element as

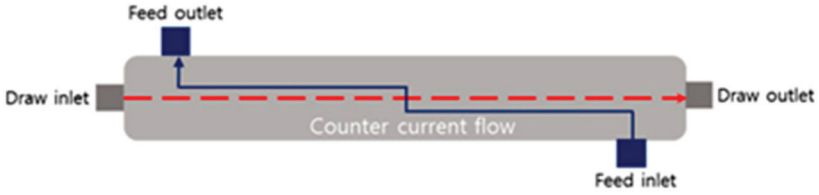


Fig. 1. SWFO PVC vessel with four ports.

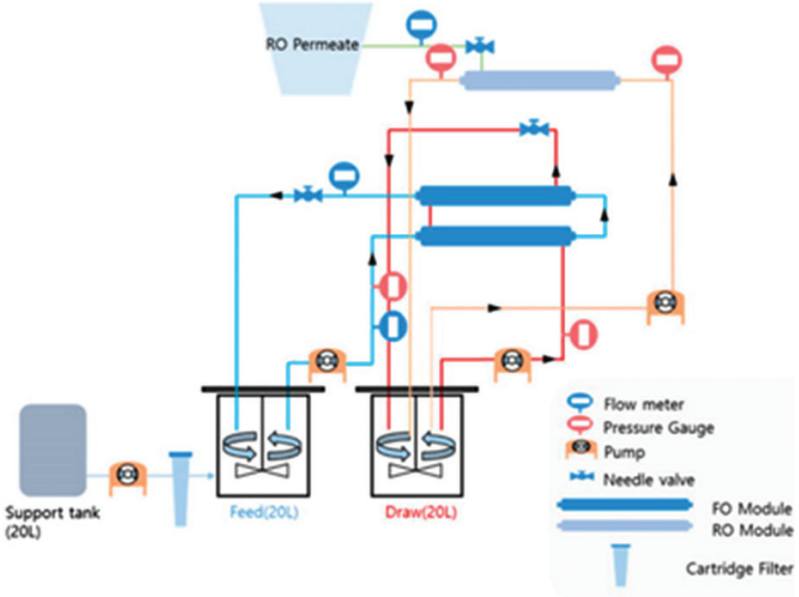


Fig. 2a. Schematic diagram of the FO–RO pilot system

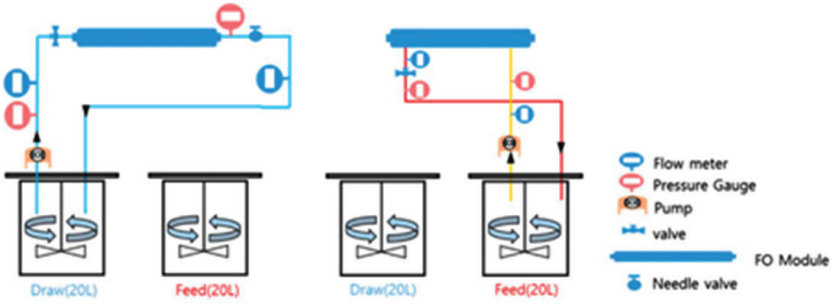


Fig. 2b. Schematic diagram of the one–stage SWFO element.

shown in Fig. 2c, meaning that the draw solution was diluted and the feed solution was concentrated one more time in the second stage of the two-stage mode. In the one-stage mode, only one osmotic dilution worked through the single SWFO element. Shortly after the operation, the retention time and dilution effect inside the element were different at each stage mode. Pressure transmitters, conductivity meter (Orion 4 Star, Thermo Scientific, Albany, USA), flow meter (feed side), and mass cylinder (draw side) were installed to measure the pressure, conductivity, flow rate, and RSF, respectively. An electronic balance (Portable Bench, CAS, Korea) was installed under the feed and draw solution tanks to measure water flux. The flow rate and pressure were controlled with an inverter installed on both sides of the solutions. All data were recorded at four min intervals. An agitator was installed on both sides of the tanks to maintain the concentration in the tank. The tank volume was 20 L. The experiment was stopped when the volume of feed solution tank decreased below 50%. At the end of every experiment, physical cleaning was conducted to remove salt deposition onto the FO membrane surface.

2.3. Water flux, reverse salt flux (RSF), and recovery rate measurement

Eq. (1) was used to calculate water flux:

$$Jw = \frac{\text{Initial food weight (kg) - Feed weighr (kg)}}{\text{Test time (min)} \times 60\text{ (min)} \div \text{Effective membrane area (m}^2\text{)}} \quad (1)$$

In Eq. (2), RSF was determined by measuring the conductivity meter installed inside the feed tank. RSF was converted to NaCl concentration using a predetermined conductivity calibration curve vs. NaCl concentration

$$J_S = \frac{C_t V_t - C_0 V_0}{A_t} \quad (2)$$

In the above equation, the C0 and Ct are the concentrations of NaCl in the feed tank at time (0) and certain time (t), respectively; whereas V0 and Vt were the volume of feed tank at time (0) and at time (t), respectively. The recovery rate was calculated using the following Eq. (3) [9]:

$$\text{Recovery (\%)} = \frac{Q_{\text{Permeate}}}{Q_{\text{Feed}}} \quad (3)$$

where QfeedandQpermeate are the feed rate and permeate flow rate(LPM), respectively.

2.4. Test conditions of the SWFO element test

The SWFO element test was conducted under various operating conditions (Table 1) To analyze FO performance, the solution concentration and array type were changed under certain conditions. All tests were carried out at room temperature. DI water and NaCl solution (Samchun chemicals, Korea) were used as feed solution and draw solution, respectively.

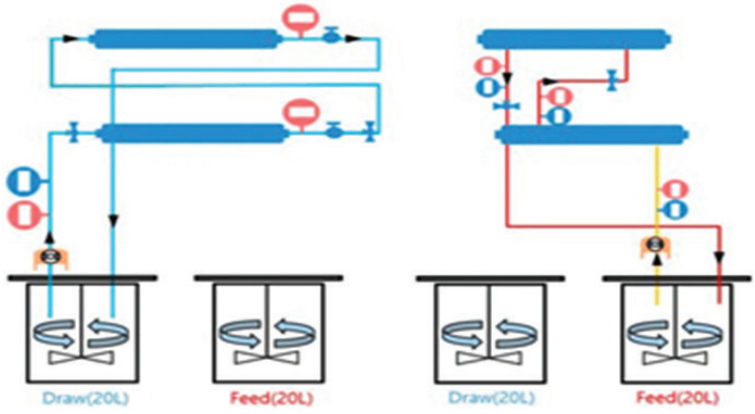


Fig. 2c. Schematic diagram of the two-stage SWFO element.

3_RESULTS AND DISCUSSION

3.1. Performance of SWFO element compared to flat sheet FO membrane

Water flux and RSF of flat sheet FO membrane and SWFO membrane in AL-facing-FS mode (FO mode), as a function of draw solution, are shown in Fig. 3. The water flux and RSF increased logarithmically when the draw solution concentration was increased. This could be due to CP phenomenon, such as dilutive internal CP and concentrative external CP [10,22,23].

Table 1. SWFO element of pilot experiments

Feed flow rate (LPM)	3.3 – 6.6
Draw flow rate (LPM)	0.35 – 0.55
Draw solution concentration (ppm)	25,000 – 70,000
Feed solution	DI water
Draw solution	NaCl solution
Array type	One stage (parallel array) Two stage (series array)
Operating temperature (℃)	21 – 23

Interestingly, when the results in Fig. 3(a) and (b) were compared, water flux in the lab-scale test was twice higher than that in the SWFO element test. This may be explained by the following: first, no significant dilution effect occurred in membrane channel in the lab-scale test compared to that in the pilot-scale test because SWFO membrane had a long flow path for draw solution. In addition, the draw solution was consistently diluted along the pathway, thus losing driving force (osmotic pressure) [12]. Therefore, the dilution level of the draw solution in the lab-scale experiment was different from that in the pilot-scale test. To mitigate this phenomenon, we recommend that a counter-current flow path may be more efficient than co-current [12,24].

Second, The SWFO element membrane has a dead zone [24,25]. This is because the SWFO flow path inside of the draw solution has a winding structure. An illustration of the SWFO element is depicted in Fig. 4 [10]. In this illustration, a dead zone is formed in the edge of the draw flow path. Because of this dead zone, the membrane effective area decreased, thus decreasing the water flux. According to previous studies [6,10,15], an increased flow rate on both sides can play a positive role in the water flux due to reduced CP effect and the enhanced mass transfer coefficient. However, a spiral-wound membrane applied in real plant process, can not only form the dead zone, but also can have different dead zone shape if the flow rate changes. Therefore, different results between lab-scale and SWFO element test were found.

Third, the SWFO element had a different water flux distribution by membrane region because membranes were rolled-up around the main draw solution pipe with different effective membrane

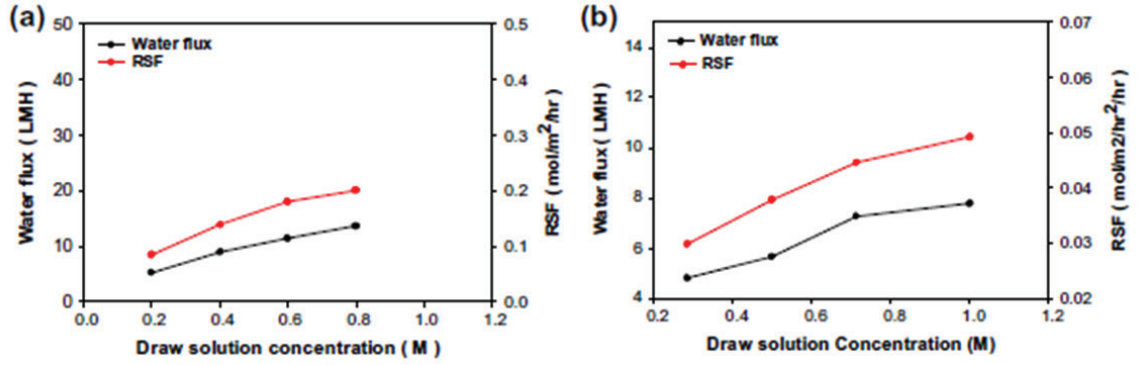


Fig. 3. Water flux and RSF comparison of two membranes with different shapes and sizes at varying draw solution concentrations: (a) Lab-scale flat sheet FO membrane test. The flow rate at both sides was 0.4 LPM at 25℃. The membrane area was 20.02 cm2 and (b) The SWFO element test. The feed rate and draw flow rate were maintained constantly at 3.3 and 0.35 LPM, respectively. The membrane area was one m2.

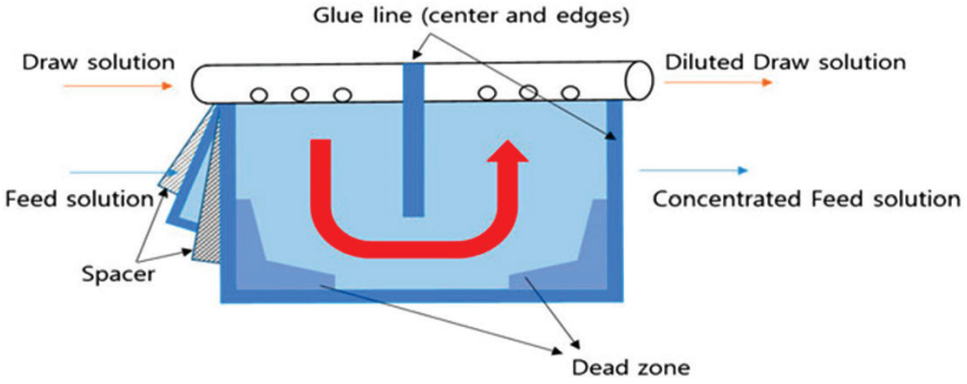


Fig. 4. An illustration of flow path and SWFO component element. Draw solution and feed solution flowed into the main pipe and space between membranes. Spacers were used both inside and outside the membrane [10,16].

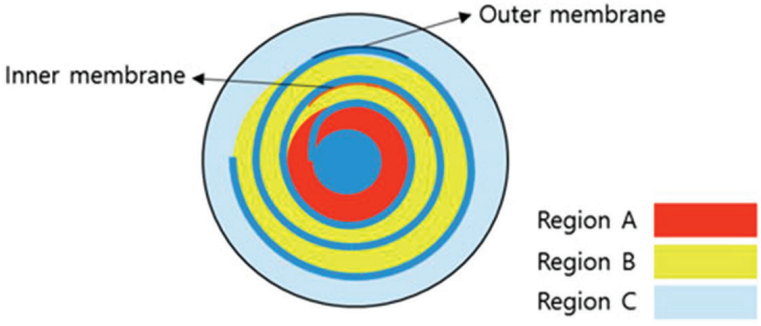


Fig. 5. Structure characteristics of Winding SWFO membrane.

areas (Fig. 5). In the regions of A and C, only the inner or outer membrane had contact with the draw solution. However, in the region of B, both inner and outer membranes contacted the draw solution. According to previous studies, region B has lower water flux than region A and C. In other words, SWFO has heterogeneity in water flux by region. Therefore, the SWFO system showed poor performance compared to flat sheet membranes, suggesting that the SW structure feature is not suitable for the FO process, consistent with findings of other studies [9,25].

Fourth, there was difference in test conditions between the two tests. In the lab-scale test, the flow rate of both sides of the solution was maintained. However, in the pilot-scale test, it was impossible to adjust the flow rate of the draw solution to that of the feed solution. This will be further discussed in the next section in detail.

3.2. Spiral-wound structure characteristics

Many FO tests using flat sheet FO membranes have been operated at the same flow rate for either side of solution because the flat sheet type membrane has a minimal pressure drop [21,22,24]. However, in the real field of membrane process, SWFO elements are connected to compose a multi-stage array. The draw solution is larger than the feed solution at the end of the element. As mentioned earlier, the SWFO membrane has special structure configuration compared to the flat sheet membrane. Therefore, it is necessary to identify the effects of the SWFO membrane structure characteristics on FO performance. In this section, we investigated the effect of SWFO structure on the flow rate and pressure on either side of the solution.

With fixed flow rate of the draw solution, the feed solution flow

rate was changed (Fig. 6(a) and (b)). This test method was used in other cases in the same manner (change of draw solution flow rate with a fixed feed flow rate). When we changed the feed solution flow rate, the draw solution flow rate decreased from 0.525 to 0.462 LPM (about 10% decrease, Fig. 6(a)). When we changed the draw solution flow rate, the feed solution flow rate dropped from 6.8 to 6.6 LPM (3% decrease, Fig. 6(b)). These results indicate that the feed solution flow rate changes significantly affected the draw solution flow rate. However, the effect of draw solution flow rate change was minimal. Similar results have been reported in previous studies [16,26,27]. Figs. 4 and 5 can be used to explain this result. The draw flow path is spiral, but the feed flow path is straight. The pressure drop can develop more severely on the draw side compared to that on the feed side. Therefore, the feed side solution can pressurize against the draw flow path at the end side of element.

In addition, the pressure of the feed side is always higher than that of the draw side in SWFO, preventing excess pressure on the draw side over that of the feed side (prevention of PRO mode). This feature can also pressurize the draw flow path. Due to these reasons induced by structural characteristics and operating conditions, the feed solution can significantly influence the draw solution.

We also investigated the relationship between inlet pressure and flow rate according to the type of element array. Results are shown in Fig. 6(c). In this experiment, a pump inverter controlled only one side of the flow. Tap water was used as feed solution and draw solution. Flow rate increased as the inlet pressure increased (inlet pressure was proportional with the flow rate) for both stage modes. The flow rate increased on the feed side more than on the draw side.

For example, when the inlet pressure on the feed side was adjusted to 0.2 bar, the feed flow rate was 5 LPM. However, the draw flow rate did not reach one LPM at the same inlet pressure. When the two-stage and the one-stage modes were compared to each other, the one stage mode was significantly influenced by the inlet pressure change, meaning that greater pressure drop in the two-stage mode interrupted the flow rate change through the two-stage series connection. In addition, when we applied the same inlet pressure, the two-stage mode had a decreased flow rate compared to the one-stage mode. As mentioned earlier, this result was due to a high-pressure drop on the draw side.

Therefore, it was impossible to adjust the flow rate element scale

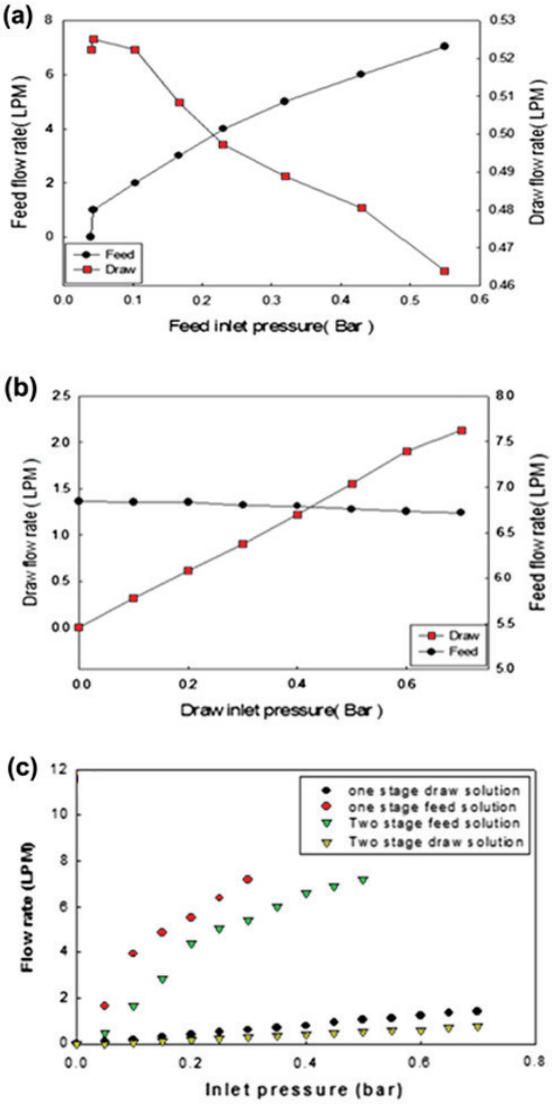


Fig. 6. Flow rate change curve of the SWFO structure (no osmotic difference between feed and draw sides of the membrane): (a) feed solution flow rate change, (b) draw solution flow rate change, and (c) comparison of the two and one-stage modes.

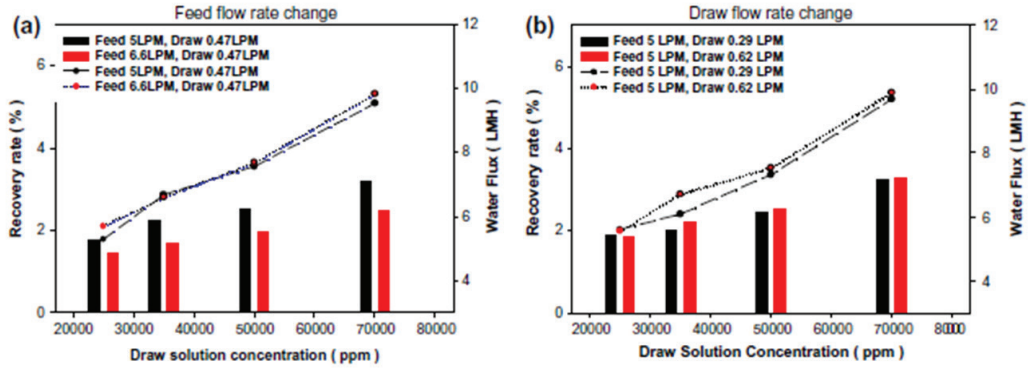


Fig. 7. Effect of feed and draw flow rates on water flux and recovery rate in the one-stage mode of the SWFO element: (a) effects of feed flow rate change (5, 6.6 LPM) when draw flow rate is fixed at 0.47 LPM, (b) effects of draw flow rate change (0.29, 0.62 LPM) when feed flow rate is fixed at 5 LPM. The pressure difference between feed inlet and draw inlet was maintained at 0.2-0.3 bar (manufacturer's recommendation). The feed inlet pressure was maintained under one bar. The draw inlet pressure was maintained under 0.7 bar. All experiments were stopped when the volume of the feed solution was half reduced.

and array type. In most membrane proequally on both sides of the SWFO element. cesses, multi-stack elements are used for water treat-In general, energy consumption and pressure in ment and desalination [11,16,28]. Therefore, we need the membrane process have great correlations with to study element scales and array types in detail.

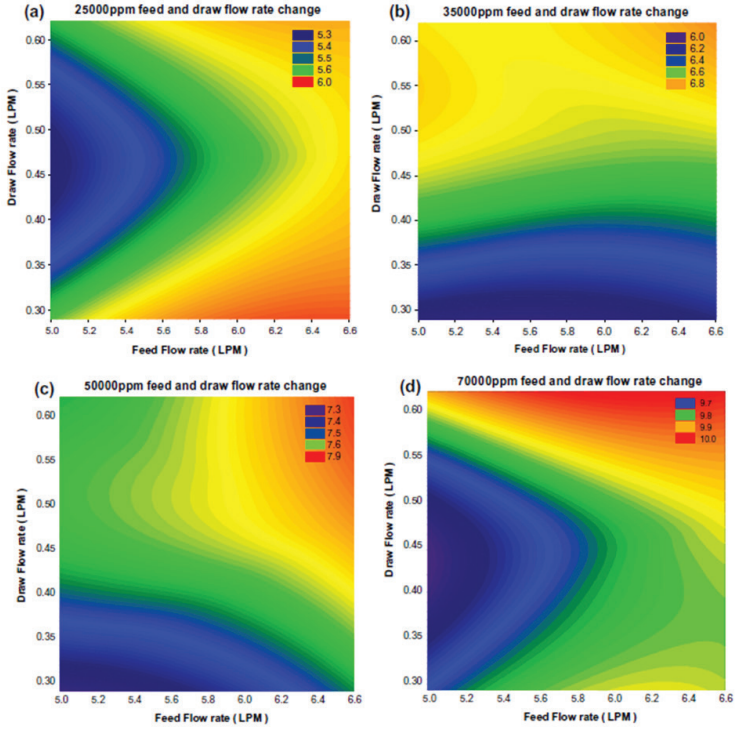


Fig. 8. Effect of the flow rate on water flux trend at varying draw solution concentrations in the one-stage mode: (a)25,000 ppm, (b) 35,000 ppm, (c) 50,000 ppm, and (d) 70,000 ppm. Color represents mean water flux. Blue colors represent low water flux while red colors represent high water flux.

3.3. Impact of flow rate change on water flux and recovery rate–one-stage mode (parallel array)

Water flux has a close relationship with recovery rate. Increases in water flux and recovery rate can reduce the membrane area and the requirement for the total number of SWFO elements in real pilot plant. This means that high water flux and recovery rates can reduce CAPEX. In this study, the effect of flow rate on water flux and recovery rate in the one-stage SWFO process was evaluated at varying draw solution concentrations. The water flux and recovery rate curves are shown in Fig. 7. As shown in Fig. 7(a),

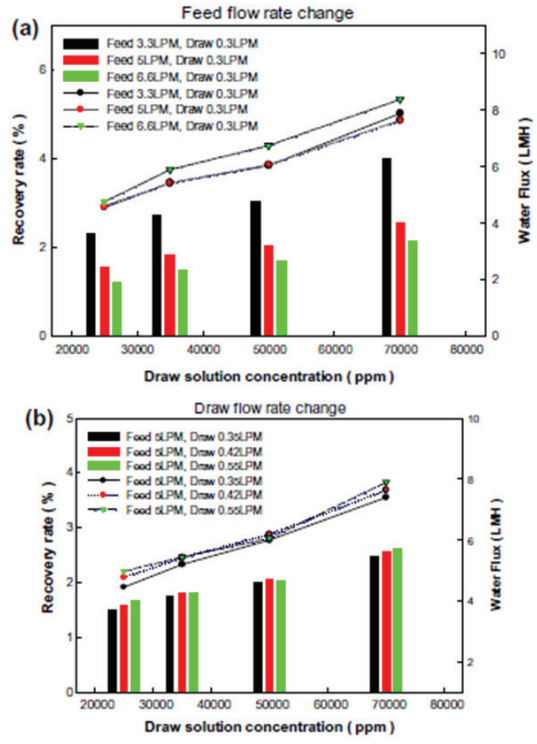


Fig. 9. Effect of feed flow rate and draw flow rate on water flux and recovery rate in the two–stage mode of the SWFO element: (a) effect of feed flow rate change (3.3, 5, 6.6 LPM) when the draw flow rate was fixed at 0.3 LPM and (b) effect of draw flow rate change (0.35, 0.42, 0.55 LPM) when the feed flow rate was fixed at five LPM. The pressure difference between the feed inlet and draw inlet was maintained at 0.2–0.3 bar (manufacturer's recommendation). The feed inlet pressure was maintained under one bar. The draw inlet pressure was maintained under 0.7 bar. All experiments were stopped when the volume of feed solution was reduced by half.

the water flux increased approximately one LMH when the feed flow rate increased from 5 to 6.6 LPM, consistent with results of previous studies [10,29,30].

Although we used DI water as feed solution, we assumed that a reverse salt diffusion could make a CECP layer on feed side. When the feed flow rate is increased, cross-flow velocity shear force can reduce the CECP layer [1,15,18]. Thus, increased feed flow rate can have a positive effect on water flux.

However, increased feed flow rate had a negative influence on the recovery rate in the performance of the one-stage SWFO membrane. The increased amount on the feed side flow rate was higher than the water flux rate (Eq. (3)). Therefore, the recovery rate decreased. This is why we need to optimize the feed flow rate considering both water flux and recovery rate [15,20]. As shown in Fig. 7(b), the water flux and recovery rate were also changed according to the draw flow rate. When the draw flow rate was increased, water flux increased due to reduced CP (DECP and DICP) and the dilution effect [23,31,32].

When the draw solution flow rate was changed, the recovery rate increased because the flow rate of the draw solution was not directly involved in Eq. (3). Therefore, the SWFO element test was affected by flow rate change on either side, meaning that FO process engineers must know the element operating conditions and membrane structure, because multi-stages element are a routine configuration in FO pilot plants.

The effect of flow rate change coming from both sides on water flux at various draw solution concentrations is shown in Fig. 8. The x-axis and y-axis represent the feed solution flow rate and draw solution flow rate, respectively. Water flux changed from five to 10 LMH, in accordance with changes in draw solution concentration. At all concentrations of draw solution, it was difficult to find consistency. This phenomenon may be due to the characteristic of pilot-scale test, making it difficult to maintain test conditions during the SWFO element test.

Despite such inconsistency, we observed that each optimized point of FO performance in different concentrations generally depended on the flow rate. At a low concentration of 25,000 ppm, the feed flow rate significantly affected water flux. However, as

the concentration increased to 35,000–70,000 ppm, water flux was significantly affected by the draw flow rate. As shown in Fig. 8(b), when the draw flow rate was at 0.4 LPM, the water flux was maintained at 6.5 LMH at all feed flow ranges, indicating that the feed flow rate had little influence on water flux in the one-stage mode.

3.4. Impact of flow rate change on water flux and recovery rate: two-stage mode (series array)

The water flux and recovery rate at varying draw concentrations with different feed and draw flow rates in the two-stage mode are shown in Fig. 9(a) and (b). These results showed a similar pattern to those in the one-stage mode. As expected, increases in both flow rate and draw solution concentration had positive effects on water flux. However, the recovery rate improved only by increased draw flow rate. Flow rate and concentration are known to have positive effects on water flux in the FO process because an increase in concentration and flow rate can cause a higher osmotic pressure difference, thus reducing the CP layer with an enhanced mass transfer coefficient [23,27].

Water flux in the two-stage mode was lower than that in the one-stage mode (parallel array). Membrane length in the two-stage mode was longer than that in the one-stage mode, causing a significant dilution effect. In the two-stage mode, two SWFO elements were connected in series (Fig. 2c), with both sides of the effluent entering the second SWFO element, indicating that the draw solution concentration of the second SWFO element was lower than that of the first SWFO element. Therefore, the osmotic pressure difference (driving force) decreased. The water flux trend in Fig. 9(a) and (b) showed that the flow rate increased, which might have reduced the CP layer and the dilution effect [6,9,10,13,15].

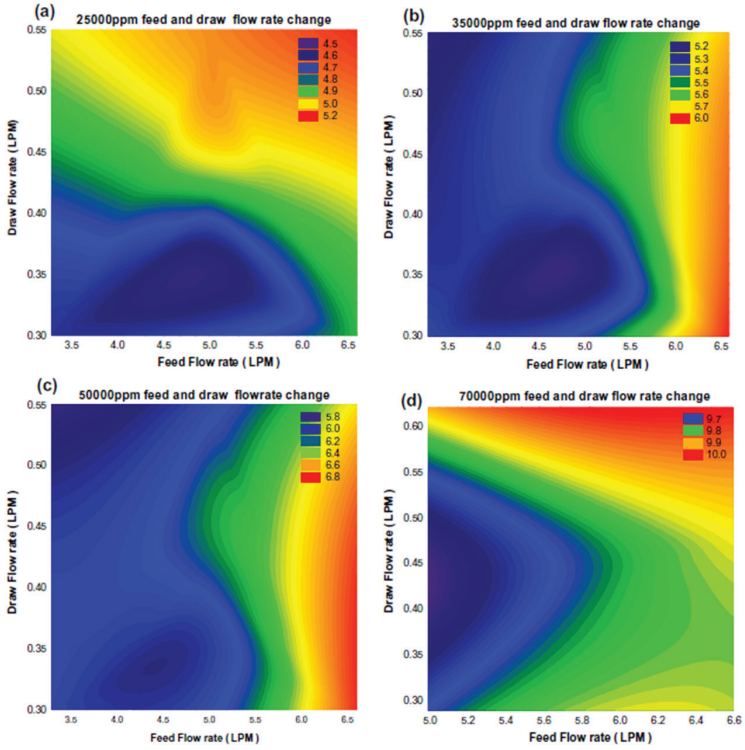


Fig. 10. Effect of flow rate on water flux trend at varying draw solution concentrations in the two–stage mode: (a)25,000 ppm, (b) 35,000 ppm, (c) 50,000 ppm, and (d) 70,000 ppm. The color represents mean water flux. Blue colors represent low water flux. Red colors represent high water flux.

In this experiment, DI water was used as feed solution, which can result in negligible CECP. However, reverse solute diffusion inevitably occurs in the FO process, leading to the increased ionic strength of the feed solution. Therefore, alternation of feed flow rate can improve the mass transport coefficient, thus increasing the water flux.

In the one-stage mode, the recovery rate was reduced by 15–20% when the feed flow rate increased.

Thus, we estimate that the recovery rate in the two-stage mode can decrease when the feed flow rate is increased, similar to the one-stage mode. However, the ratio of the recovery rate decrease with feed flow rate change in the two-stage mode was lower than that in the one-stage mode, with a decrease of approximately 30%. As mentioned above, water flux in the two-stage mode was lower than that in the one-stage mode due to the fact that recovery rate could be affected by the dilution effect and permeate flow rate (Eq. (3)).

In addition, the fixed draw flow rate was different in the two tests. In the one-stage mode, the draw flow rate was 0.47 LPM. In the two-stage mode, the draw flow rate was 0.3 LPM. The lower water flux was attributed to draw flow rate (Fig. 6). Therefore, in the process using the SWFO element, flow rate can significantly affect pressure drop, water flux, recovery rate, dilution effect, and CP.

We further studied the flow rate effects in the SWFO element test by comparing water flux as a function of the feed/draw flow rate and draw solution concentration (Fig. 10) [13,24,27,33]. Across all draw solution concentrations, water flux was generally low under the conditions of low feed rate and draw flow rate. In both tests, the effect of the draw flow rate on water flux was more obvious compared to feed flow rate because the dilution effect was minimum with a low water flux. In contrast, as the draw concentration increased, the water flux was more dependent on feed solution than draw solution (Fig. 10(b), (c), and (d)).

In addition, the membrane support layer is an unstirred layer unaffected by flow rate or reduced DICP [15,17]. However, in this study, ionic strength in feed solution was found to be an important factor for water flux, which is in agreement with previous reports [2,11]. Although DI water was used as feed water, the ionic strength increased with RSF. This test lasted until concentration rate reached two ionic strengths of nearly 3 mS/cm at the end of the test. RSF was increased as a function of concentration gradient [23,34]. Thus, it is expected that the RSF will increase when the draw solution concentration increases [23,34].

In element scale SWFO test, the water flux and RSF significantly diluted the draw solution, resulting in concentrated feed solution. High RSF at a high draw solution concentration might have caused CECP on the membrane surface layer. The feed flow rate might have affected the removal of the CECP layer. In the two-stage mode, both sides of solution stayed inside the element longer than in the one-stage mode. Therefore, the ionic strength of the feed side significantly increased. Consequently, the increase in flow rate of the feed solution affected water flux at high draw concentrations.

4_CONCLUSIONS

In this study, we found that the results from a labscale test could not be directly applied in a pilot-scale plant. The effect of element structural characteristics, array, and flow rate on SWFO performance was determined. We summarized the results as follow:

1) A spiral-wound element is different from a flat sheet membrane in structural configuration, causing a significant pressure drop due to its draw flow path, which was longer and more tightly wound than the feed flow path. In addition, the effective membrane area was reduced due to formation of dead zone area.

2) The increased flow rates on both sides of the membrane had a positive effect on the membrane surface by increasing shear forces (mass transfer coefficient), thus reducing the effect of dilution CP.

3) Based on the results of our tests according to the types of array (one- and two-stage modes), solution retention time was different due to SWFO structural characteristics. In the twostage

mode, a long retention time and increased ionic strength significantly affected FO performance, which was why the feed flow rate affected water flux more than the draw flow rate.

Therefore, before commercialization, a pilot-scale test regarding operating conditions such as draw solution concentration, flow rate, and the type of element array, must be conducted.

ACKNOWLEDGEMENT

This research was supported in part by a grant (code 15IFIP-B088091-02) from the Industrial Facilities and Infrastructure Research Program funded by Ministry of Land, Infrastructure and Transport of the Korean government. This research was also supported in part by the Korean Ministry of Environment (MOE), as a Knowledge-based environmental service (Waste to energy recycling, Eco design) and the Human resource development Project.

REFERENCES

1. Q. Yang, K.Y. Wang, T.-S. Chung, Dual-layer hollow fibers with enhanced flux as novel forward osmosis membranes for water production, Environ. Sci. Technol. 43 (2009) 2800–2805.
2. G. Blandin, A.R.D. Verliefde, C.Y. Tang, P. Le-Clech, Op portunities to reach economic sustainability in forward osmosis–reverse osmosis hybrids for seawater desalination, Desalination 363 (2015) 26–36.
3. L.F. Greenlee, D.F. Lawler, B.D. Freeman, B. Marrot, P. Moulin, Reverse osmosis desalination: Water sources, technology, and today's challenges, Water Res. 43 (2009) 2317–2348.
4. R. Semiat, Energy issues in desalination processes, Environ. Sci. Technol. 42 (2008) 8193–8201.
5. C. Fritzmann, J. Lo¨wenberg, T. Wintgens, T. Melin, State-of-the-art of reverse osmosis desalination, Desalination 216 (2007) 1–76.
6. S. Chakrabortty, M. Pal, M. Roy, P. Pal, Water treatment in a new flux-enhancing, continuous forward osmosis design: Transport modelling and economic evaluation towards scale up, Desalination 365 (2015) 329–342.
7. R. Valladares Linares, Z. Li, M. Abu-Ghdaib, C.-H. Wei, G.Amy,J.S. Vrouwenvelder, Water harvesting from municipal wastewater via osmotic gradient: An evaluation of process performance, J. Membr. Sci. 447 (2013) 50–56.
8. T. Cath, A. Childress, M. Elimelech, Forward osmosis: Principles, applications, and recent developments, J. Membr. Sci. 281 (2006) 70–87.
9. D. Attarde, M. Jain, K. Chaudhary, S.K. Gupta, Osmotically driven membrane processes by using a spiral wound module —Modeling, experimentation and numerical parameter estimation, Desalination 361 (2015) 81–94.
10. Y.C. Kim, S.J. Park, Experimental study of a 4040 spiral -wound forward-osmosis membrane module, Environ. Sci. Technol. 45 (2011) 7737–7745.
11. N.T. Hancock, P. Xu, M.J. Roby, J.D. Gomez, T.Y. Cath, Towards direct potable reuse with forward osmosis: Technical assessment of long-term process performance at the pilot scale, J. Membr. Sci. 445 (2013) 34–46.
12. Y. Sato, S.-I. Nakao, Theoretical estimation of semipermeable membranes leading to development of forward osmosis membranes and processes as a future seawater desalination technology, Desalin. Water Treat. 57(12) (2016) 5398–5405.
13. A. Achilli, T.Y. Cath, A.E. Childress, Selection of inorganic -based draw solutions for forward osmosis applications, J. Membr. Sci. 364 (2010) 233–241.
14. E. Nagy, A general, resistance-in-series, salt- and water flux models for forward osmosis and pressureretarded osmosis for energy generation, J. Membr. Sci. 460 (2014) 71–81.
15. J.E. Kim, S. Phuntsho, F. Lotfi, H.K. Shon, Investigation of pilot-scale 8040 FO membrane module under different operating conditions for brackish water desalination, Desalin. Water Treat. 53 (2014) 2782–2791.
16. J. Schwinge, P.R. Neal, D.E. Wiley, D.F. Fletcher, A.G. Fane, Spiral wound modules and spacers, J. Membr. Sci. 242 (2004) 129–153.
17. J. Fa´rkova´, The pressure drop in membrane module with spacers, J. Membr. Sci. 64 (1991) 103–111.

18. S. Sundaramoorthy, G. Srinivasan, D.V.R. Murthy, An analytical model for spiral wound reverse osmosis mem brane modules: Part I—Model development and parameter estimation, Desalination 280 (2011) 403–411.
19. A. Da Costa, A. Fane, D. Wiley, Spacer characterization and pressure drop modelling in spacer-filled channels for ultrafiltration, J. Membr. Sci. 87 (1994) 79–98.
20. Z. Cao, D. Wiley, A. Fane, CFD simulations of nettype turbulence promoters in a narrow channel, J. Membr. Sci. 185 (2001) 157–176.
21. M. Shibuya, M. Yasukawa, T. Takahashi, T. Miyoshi, M. Higa, H. Matsuyama, Effect of operating conditions on osmotic-driven membrane performances of cellulose triacetate forward osmosis hollow fiber membrane, Desalination 362 (2015) 34–42.
22. C. Kim, S. Lee, S. Hong, Application of osmotic backwashing in forward osmosis: Mechanisms and factors involved, Desalin. Water Treat. 43 (2012) 314–322.
23. W.A. Phillip, J.S. Yong, M. Elimelech, Reverse draw solute permeation in forward osmosis: Modeling and experiments, Environ. Sci. Technol. 44 (2010) 5170–5176.
24. B. Gu, D.Y. Kim, J.H. Kim, D.R. Yang, Mathematical model of flat sheet membrane modules for FO process: Plate-and-frame module and spiral-wound module, J. Membr. Sci. 379 (2011) 403–415.
25. M. Kostoglou, A. Karabelas, On the fluid mechanics of spiral -wound membrane modules, Ind. Eng. Chem. Res. 48 (2009) 10025–10036.
26. Y. Xu, X. Peng, C.Y. Tang, Q.S. Fu, S. Nie, Effect of draw solution concentration and operating conditions on forward osmosis and pressure retarded osmosis performance in a spiral wound module, J. Membr. Sci. 348 (2010) 298–309.
27. G. Schock, A. Miquel, Mass transfer and pressure loss in spiral wound modules, Desalination 64 (1987) 339–352.
28. S. Lim, H. Park, H. Lee, K. Yum, H. Lee, D. Woo, Application of seawater dilution process to SWRO filtration system for low-energy desalination, Desalin. Water Treat. 57(16) (2016) 7414–7421.
29. A. Achilli, T.Y. Cath, A.E. Childress, Power generation with pressure retarded osmosis: An experimental and theoretical investigation, J. Membr. Sci. 343 (2009) 42–52.
30. T.Y. Cath, Osmotically and thermally driven membrane processes for enhancement of water recovery in desalination processes, Desalin. Water Treat. 15 (2012) 279–286.
31. A. Sagiv, A. Zhu, P.D. Christofides, Y. Cohen, R. Semiat, Analysis of forward osmosis desalination via two-dimensional FEM model, J. Membr. Sci. 464 (2014) 161–172.
32. S. Lee, Y.C. Kim, S.-J. Park, S.-K. Lee, H.-C. Choi, Experiment and modeling for performance of a spiralwound pressure-retarded osmosis membrane module, Desalin. Water Treat. 57(22) (2016) 10101–10110.
33. Y. Kim, J.H. Lee, Y.C. Kim, K.H. Lee, I.S. Park, S.-J. Park, Operation and simulation of pilot-scale forward osmosis desalination with ammonium bicarbonate, Chem. Eng. Res. Des. 94 (2015) 390–395.
34. N.T. Hancock, T.Y. Cath, Solute coupled diffusion in osmotically driven membrane processes, Environ. Sci. Technol. 43 (2009) 6769–6775.

O_3/BAC 공정에서 후단여과막 적용성 연구

A Study on Applicability of Post membrane in O_3/BAC Process

엄정열
토목플랜트연구팀, 선임연구원
jungyeol.eom@daewooenc.com

오희경
토목플랜트연구팀, 책임연구원
pilsun.kang@daewooenc.com

본 논문은 2016년 Desalination and Water Treatment Vol.57, 2016, pp. 24583–24594에 게재되었던 논문을 재게재한 것입니다.

Abstract

This study was conducted to applicability of post membrane through the O_3/BAC process with a pilot plant installed 25m^3/day scale to the Y purification plant in S City. Chlorine demand and Chlorine decay rate(K^*C_0) were compared for post membrane and BAC filteredwater. Chlorine demand of BAC effluents at 24hr, 48 hr was 0.1mg/L and 0.15mg/L higher than the measured post membrane effluents. Also K^*C_0 values appear that chlorine decay rate was reduced by 25% more than BAC filtered water when post membrane was applied. BAC filtered water was observed by 637CFU/mL bacteria and 1.26×10^4 CFU/mL HPC. However, through the post membrane filtration process, it was observed that 0 CFU/mL bacteria and 3.8×10 CFU/mL HPC. For the comparison of particle counts, we experiment the three pattern. First Immediately after backwashing, second different filter to waste time and last using post membrane filtration. As a result, there were no particle counts difference occurred before and after backwashing with post membrane filtration process. Through this study, O_3/BAC/membrane filtration confirmed the applicability of the process.

Keywords : O_3/BAC, Post membrane, Chlorine demand, Chlorine decay rate, Bacterial numbers, Particle counts, OBM process

1_서론

최근 가속화되는 수질오염과 더불어 생활수준 향상으로 건강에 대한 관심이 증가하고 있고 자연스럽게 음용수 전체 수질에서 안전성에 대한 요구가 높아지는 추세이다. 하지만 표주정수처리공정으로 제거되지 않는 물질들로 인해 문제가 발생하여 많은 정수장에서 고도정수처리공정으로써 O_3/BAC 공정을 도입해 시민들에게 양질의 수돗물을 공급하고 있다. 고도정수처리 공정에서 사용하는 BAC는 활성탄을 재생하지 않고 3~5년 정도 사용할 수 있으므로, 경제적인 이점이 존재한다. 하지만 BAC 여과수에서 활성탄 입자 및 세균 누출로 인해서 염소소독 시 소독제 사용량의 증가, 분탄 및 탈리세균 유출로 인한 급수배관 내 2차 오염 등을 유발할 수 있으므로 반드시 제거되어야 한다. 이러한 문제점을 해결하고자 일본이 미사토, 아사카 정수장에서는 BAC 여과지 후단에 모래여과공정을 추가로 도입하였고, 캐나다의 Lakeview 정수장은 표준정수처리 공정을 OBM(Ozone, BAC, Membrane) 공정으로 전환하여 운영 중이다.

본 연구에서는 O_3/BAC 공정 후단에 여과막을 설치하여 활성탄에서 누출되는 입자, 세균 및 유기물의 제거, 염소소비속도 및 염소요구량의 비교, 역세척 후 BAC의 안정화에 대한 평가를 실시하였다. 이를 통해 O_3/BAC/Membrane 공정 적용 가능성을 평가하고자 하였다.

2_연구방법

Y정수장은 기존의 표준정수처리공정 후단에 O_3/BAC가 추가된 고도정수처리공정을 통해 시민들에게 250,000톤/일의 수돗물을 공급하고 있다. 실험에서 사용된 고도정수처리 파일럿 플랜트는 Y정수장의 모래여과수를 원수로 이용하여 O_3/BAC 공정을 파일럿 플랜트 운전하였다.(Fig.1) 시설용량은 25톤/일 규모로 Y정수장에 설치하였으며, 본 실험은 2014년 4월부터 2015년 5월까지 약 1년정도 실시하였다. 오존주입농도는 1~2mg/L, BAC의 재질은 석탄계, 접촉시간(EBCT)은 15~18min, 1~2주에 한번 역세척을 실시하였다. BAC 후단에 막면적 4m², 막여과유속 4.5m/d로 운전되는 후단여과막(post membrane) 공정을 추가로 설치하였다. 현재 운영하고 있는 파일럿 플랜트의 운전조건 및 최종여과막 모듈을 아래의 Table 1에 나타내었고, 정수장 유입 원수 및 파일럿 플랜트 유입원수의 수질자료는 Table 2에 나타내었다.

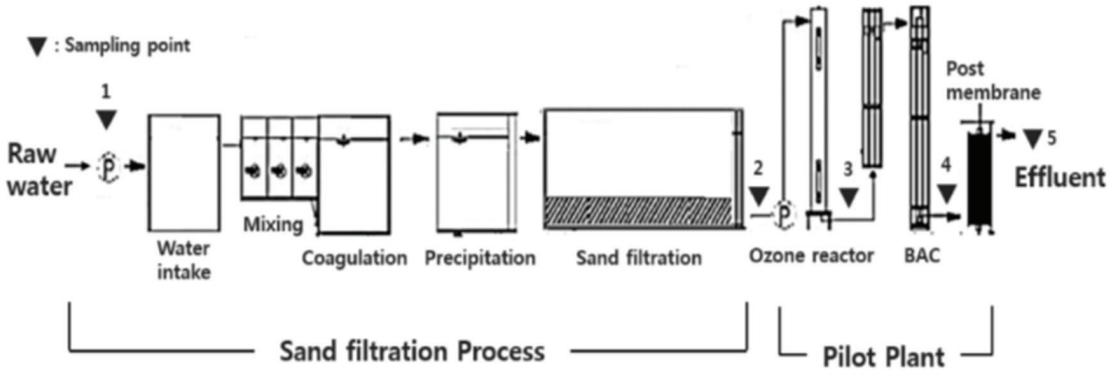


Fig. 1. Schematic diagram of water treatment process.

Table 1. Design and operation parameters for the pilot plant

Item		Design	
Flow rate		25 m³/day	
Ozonation	Contactor	300 (l) × 350 (W) × 3000 (H) mm	
	Ozone dose	1~2 mg/L	
	Contact time	15~18 min	
BAC adsorption	EBCT	15 min	
	Volume	0.208 m³	
	Depth	2 m	
	Back Washing	Water + Air	
	Back washing Time	Air	2 min
		Air + Water	30 sec
		Water	5 min
Post Membrane (MF)	Surface area	4 m²	
	Diameter	216 mm (8.5")	
	Lenght	1,120 mm	
	Material	PVDF (polyvinylidene fluoride)	
	Flux	4.5 m³/m²day	

Table 2. Characteristics of water quaility in raw water and sand filtration

	Raw water			Sand Filtration		
	Max	Min	Average	Max	Min	Average
Temperature (℃)	25.5	0.9	16.9	26.3	1.8	17.8
pH	7.63	6.78	7.21	7.8	6.9	7.35
Electric Conductivity (㎲/cm)	222.4	156.2	190.6	246.4	161.9	193.3
Alkalinity (mg/L as $CaCo_3$)	99	50.75	69.2	81	47	60.93
$KMnO_4$ (mg/L)	4.97	1.13	3.41	2.29	0.24	1.45
Turbidity (NTU)	9.63	1.59	4.11	0.21	0.11	0.16
UV_{254} (cm^{-1})	0.074	0.031	0.035	0.030	0.014	0.019
TOC (mg/L)	3.072	1.477	1.673	1.99	0.85	1.27

3_결과 및 고찰

3.1. 활성탄 공정 통과 후 특징

본 실험은 2014년 4월부터 2015년 5월까지 약 1년정도 실시하였으며, Fig. 2는 운전기간에 따른 DOC, C/C0 및 활성탄 변화를 나타낸 것이다.

A구간(GAC 설치후 120일 가량)은 운전초기에 활성탄 표면에 박테리아가 부착되는 단계로 이 시기에는 DOC제거의 대부분이 주로 물리적 흡착에 의해 이루어지는 구간이다. B구간(120~215일 가량)은 GAC의 파과가 진행되어감에 따라 DOC 흡착능이 점차 감소하고, DOC 제거는 물리적 흡착과 생물학적 분해가 동시에 일어나는 구간이다. C구간(215일~480일 가량)의 DOC, C/C0 는 대략 0.75 이상으로 이 시점에서는 활성탄의 DOC 흡착능은 상당부분 소진되었기 때문에 생물학적인 분해가 DOC 제거의 주요한 메커니즘이다. 보통 A구간은 GAC 공정, B구간과 C구간을 주로 생물활성탄공정(BAC)으로 평가한다. 활성탄 시료 채취 후 SEM을 이용하여 입상활성탄 표면을 관찰한 결과 생물막으로 보이는 피막으로 덮여 있는 것을 확인할 수 있다. 이는 BAC에 흡착되어 공급되는 영양물질들로 인해 유입수

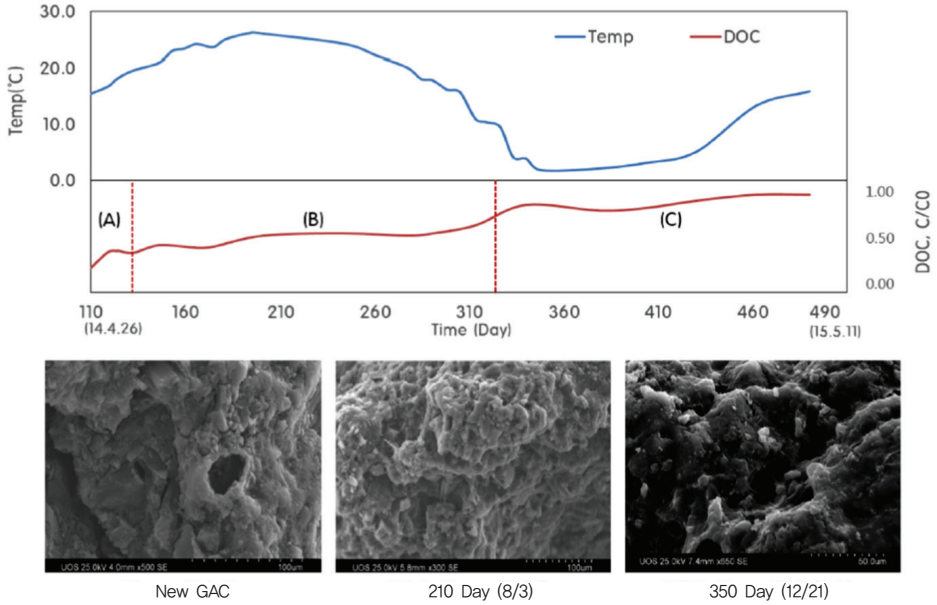


Fig. 2. Variation of DOC, C/C0 and SEM images of GAC particle during the operation periods

내의 부유성 박테리아들이 활성탄 표면에서 부착, 성장, 탈착을 반복하면서 군집 및 생물막을 형성하기 때문이다.

3.2. FEEM을 통한 정수처리 공정별 유기물 특성

Fig 3은 정수처리에서 각 공정별 FEEM 측정 결과를 나타내고 있다. 모래여과수에서는 Aromatic protein(A), Fulvic acid(B), Tryptophan protein-like(C) 그리고 Humic acid(D)가 전체적으로 높게 검출되었다. 하지만 O3 공정을 거치고 나서 A, B, C 그리고 D의 Peak가 각각 83.6%, 52.1%, 90% 그리고 69.2% 감소한 것을 확인할 수 있었다. 이는 오존이 이중결합 혹은 방향성 구조를 가지는 유기물의 구조를 변형시키거나 직 · 간접적인 산화작용으로 유기물을 제거한 것으로 보인다.

또한, BAC 공정을 거치면서 Peak D 부분인 Humic acid가 47% 감소되고, Peak B 부분인 Fulvic acid가 34.8% 제거된 것을 확인할 수 있는데, 이는 흡착 혹은 생물학적분해를 통해서 제거되기 때문으로 판단할 수 있다. BAC 공정 후단에 설치한 여과막을 거치면서 Peak C 부분인 Tryptophan protein-like는 37.9%가 제거되었고, Peak A 부분인 Aromatic protein는 22.2%가 제거되었다는 것을 알 수 있었다.

3.3. 염소소비속도 및 염소요구량

3.3.1 공정별 염소소비속도 및 염소요구량 비교

Fig. 4는 플랜트에서 원수, 모래여과, 오존, BAC 여과수 및 후단여과막 처리수에서의 염소소비속도상수 및 염소요구량을 나타낸 그림이다. BAC 여과수 및 후단 여과막 처리수에서는 k*C0 값이 감소하는 것을 볼 수 있으나, 오존 공정에서는 k*C0 값이 모래여과수 대비 15% 증가한 것을 관찰할 수 있었다. Fig. 4, 5를 살펴보면, 이는 오존에 의한 영향이라고 추측할 수 있다. 기존 연구결과에 의하면 오존처리는 겉보기 분자량의 감소, 방향성 감소, 카르복실기 작용기 증가, 지방산, Alkanes의 증가 등의 유기물 특성변화를 가져오는 것으로 보고되고 있으며, Fig. 3과 같이 오존으로 인해서 Aromatic, Fulvic, Humic, Trytophan Pro-

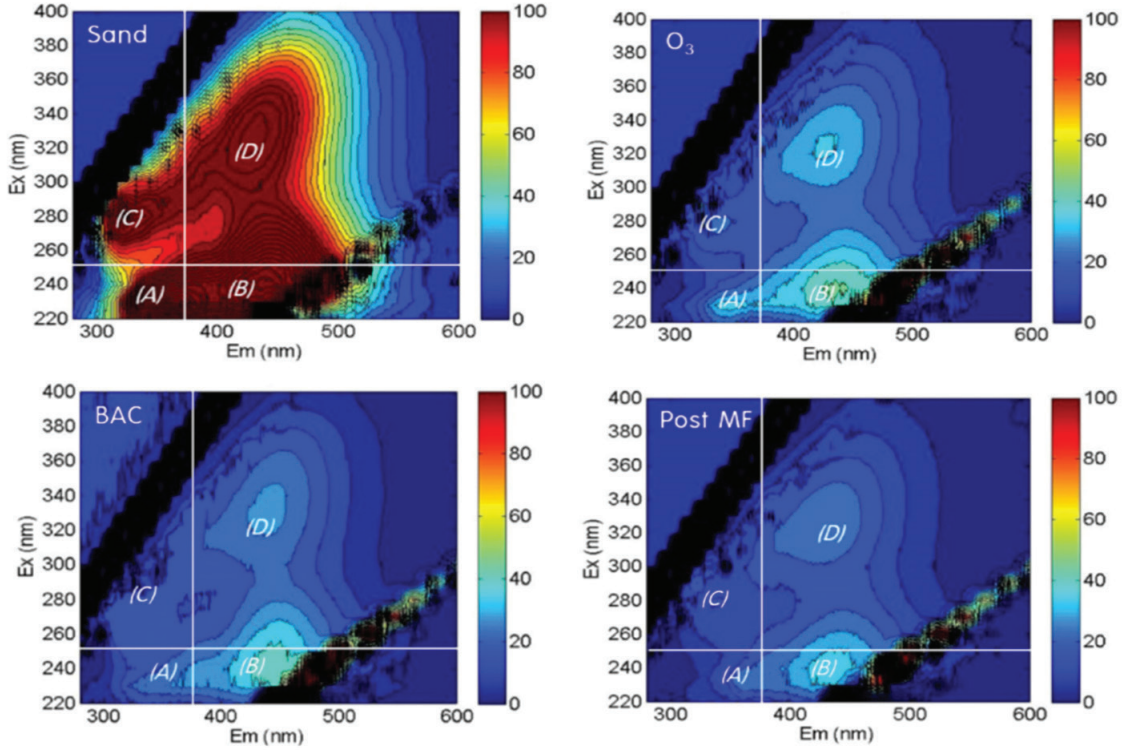


Fig. 3. Characteristics of organic substance by FEEM : Sand, Ozone, BAC, and Post MF.

tein-like 등이 변화하는 것을 확인할 수 있었다. 이는 오존 공정을 통해 분해 가능한 유기물이 증가하여 낮은 유기물 농도에도 불구하고 K*C0 값이 높게 나타나는 것으로 판단된다. Fig. 4를 통해 후단여과막 처리수의 염소소비 속도가 BAC 여과수보다 25% 감소하고, 24hr와 48hr의 염소요구량이 BAC 여과수보다 20%, 25% 감소하는 것을 볼 수 있다.

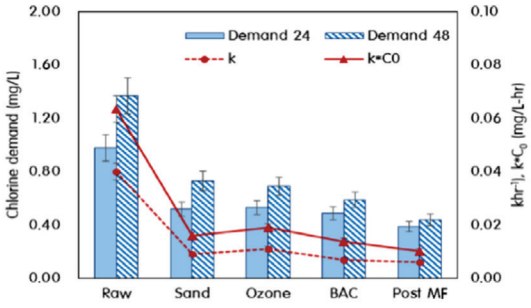


Fig. 4. Chlorine decay rate and chlorine demand in each process.

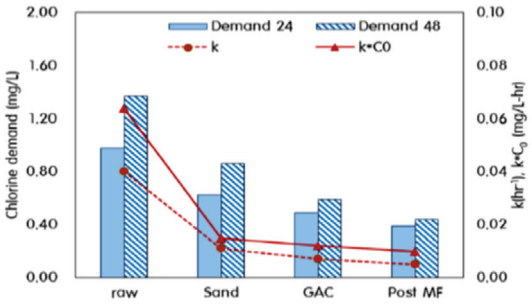


Fig. 5. Chlorine decay rate and chlorine demand in each process(Exception of ozone process).

3.3.2 온도별 염소소비속도 및 염소요구량

염소유구량 및 염소소비속도에 대한 수온의 영향을 살펴보기 위해 BAC 여과수와 후단여과막 처리수에 대한 수온을 5℃, 15℃, 25℃로 변화시키면서 실험을 실시하였다. Fig. 6과 같이 후단여과막 처리수에서 염소소비속도는 5℃에서 0.008hr^{-1}, 15℃에서 0.011hr^{-1} 25℃에서 0.021hr^{-1} 로 BAC 여과수와 비교하여 각각

11.1%, 20.8%, 22.2%가 감소하였다. 또한, BAC 여과수에 비해 후단여과막 처리수의 염소요구량은 5℃ 24hr에서 14.3%, 48hr에서 13.1%, 15℃ 24hr에서 3.1%, 48hr에서

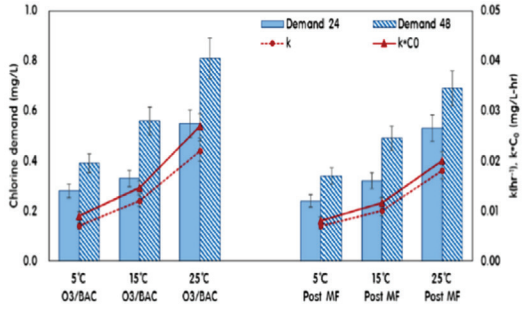


Fig. 6. Chlorine decay rate and chlorine demand in each temperature.

14.3%, 25℃에서 24hr에서 2.8%, 48hr에서 16.7% 감소하는 것을 확인할 수 있었다. BAC 여과수와 비교하면 후단여과막을 적용한 경우 후염소 주입량이 20~25% 정도 절감가능하고, 수온변화에 따른 염소소비속도 및 염소요구량의 감소가 크지 않다는 것을 알 수 있다. 이를 통해서 후단여과막 적용시 급수계통에서 잔류염소 안정화에 도움이 될 것으로 판단된다.

3.4. 미생물 개체수 변화

플랜트 공정에서 발생하는 일반세균 및 저온일반세균(HPC)을 관찰하였다. 2014년 6월부터 2015년 5월까지 11개월간 공정별, 기간별 일반세균을 측정하였다. (Table 3)

Table 3. Bacterial counts on each process (CFU/mL)

	1st (14.06.11)	2nd (14.10.21)	3rd (14.11.26)	4th (15.03.13)	5th (15.04.23)	6th (15.05.11)
Sand filtration	6	2	5	7	11	46
O_3	0	0	0	1	3	2
BAC	27	47	144	196	312	637
Post MF	0	0	0	0	0	0

6월의 BAC 여과수에서 일반세균 27CFU/mL를 확인할 수 있었는데, Flg. 2에서 확인한 바와 같이 이 시기에는 BAC로 전환되는 과정 중이므로 일반세균이 적게 관찰된 것으로 판단된다. 11월에는 수온이 10℃ 이하이지만 일반세균 144CFU/mL가 관찰되었는데, 이는 BAC로 전환되었기 때문에 낮은 온도에도 높은 수치를 보인 것으로 판단되었다. 3월에는 196CFU/mL를 관찰할 수 있었는데 이는 수온이 10℃이하여서 미생물이 크게 성장하지 않았기 때문으로 판단할 수 있었다. 4월과 5월로 진행되면서 수온증가로 인해 BAC에서 일반세균이 증가하는 것을 관찰할 수 있었다.

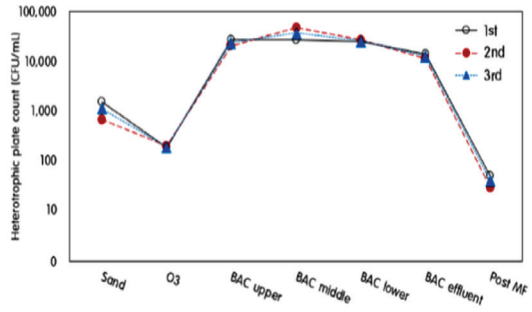


Fig. 7. Changes in heterotrophic plate counts in each process

공정별 저온일반세균(HPC)의 결과는 Fig. 7에 나타내었다. Table 3의 결과를 바탕으로 일반세균이 300CFU/mL 이상 나온 4월부터 5월까지 실험을 진행하였다. 모래여과수에서 HPC는 평균적으로 1.09×10^{3}CFU/mL가 관찰되었고, 오존공정을 거치면서 1.85×10^{3}CFU/mL가 관찰되었는데, 이는 오존이 미생물 및 세균에 영향을 끼쳤기 때문으로 판단된다. 선행연구자들에 의하면 오존처리가 박테리아의 막을 파괴하고, 단백질을 공격하여 핵산을 용출시키며 DNA를 불활성화시킴으로써 바이러스의 불활성화를 일으키는 것으로 보고하였다. 오존공정을 거친 후 BAC 여과조의 깊이별 유출수에서 HPC를 측정하였다. Upper 부분(175cm)에서는 2.38×10^{3}CFU/mL, Middle 부분(110cm)에서는 3.7×10^{3}CFU/mL, Lower 부분(45cm)에서는 1.2×103CFU/mL의 값을 얻었다. 하지만 후단여과막공정을 거치고 나서 3.8×10^{3}CFU/mL의 값을 얻었는데, 이를 통해서 BAC에서 유출된 미생물(Upper~BAC 유출수 평균값)이 후단여과막을 거치면서 99.84% 제거된다는 것을 확인할 수 있었다.

3.5. BAC 여과수의 염소소독평가

운영중인 O_3/BAC 공정의 최종처리수에 세균이 부착된 활성탄 입자가 누출되었을 때, 활성탄 내 세균 및 미생물의 염소소독 저항성 평가를 하였다. Table 4의 결과에서 알 수 있듯이 활성탄이 있는 물을 염소소독한 경우가 활성탄을 초음파 처리한 후 염소 소독한 경우보다 세균수가 높게 나타났는데, 이는 기존의 연구결과와 마찬가지로 활성탄 입자의 표면이나 갈라진 틈이 미생물의 은신처 역할을 함으로서 염소소독으로부터 보호되기 때문으로 추정할 수 있다. 활성탄에 부착되어 있던 세균들 중 염소 소독내성이 강한 세균이 내/외부의 충격에 의해 탈리되어 배 · 급수관으로 유입이 되거나, 역세척 직후 초기 누출입자에 포함될 가능성이 있으나 BAC 공정 후단에 여과막을 설치함으로써 이러한 문제점을 해결할 수 있을 것으로 판단할 수 있다.

3.6. BAC 역세척 전/후 입자물질의 누출 평가

Table 5는 모래여과수, BAC 여과수, 후단여과막 처리수의 안정기의 입자수를 비교한 것이다. 모래여과수에 비해 파일럿 플랜트에서 생산된 BAC 여과수는 2um 이하 입자수가 큰 차이를 보이는 것을 확인하였다. 이러한 결과는 생물활성탄의 분탄, 탈리세균 및 미세플럭 등의 누출에 의한 것

Table 4. Results of heterotrophic plate counts after chlorination

	Before sonication	After sonication
Bacteria (CFU/g GAC)	3.5×10^{3}~2.4×10^{5}	1.2×10^{2}~1.8×10^{4}

Table 5. Comparison of particle counts and turbidity before backwashing in each process (Counts/mL)

Particle size / Process	2.0 μm	5.0 μm	10.0 μm
Sand filtration	7~62	<10	<5
BAC effluent	21~111	<10	<8
Post MF effluent	3~6	<1	<0

	Sand filtration	BAC effluent	Post MF effluent
Turbidity (NTU)	0.11~0.21	0.05~0.08	0.02~0.04

이라고 판단되었다. 기존 고도정수처리 공정 후단에 여과막 공정을 설치한 후 2um 이하 입자수를 확인한 결과 3~6개/mL의 입자수가 누출되는 것을 확인하였다. 이를 통해서 BAc 공정 후단에 여과막공정을 설치할 경우 입자누출에 대한 안전성을 확보하는 동시에 수돗물의 신뢰도를 높이는 방법이 될 것으로 판단된다.

Table 6. Comparison of particle counts and turbidity before backwashing in each process (Measured at 5min later after backwashing) (Counts/mL)

Particle size / Process	2.0 ㎛	5.0 ㎛	10.0 ㎛
BAC effluent	<3500	<120	<25
Post MF effluent	<5	<0	<0

	BAC effluent	Post MF effluent
Turbidity (NTU)	0.65~1.2	0.02~0.04

BAC 여과지 안에서는 미생물증식 및 생물막 형성만 발생하는 것이 아니라, 무기물질도 함께 축적된다. 축적된 무기물질은 손실수두를 증가시키고, 영양물질이 생물막으로 확산하는 것을 방해하기 때문에 역세척을 반드시 실시해야 한다. 하지만 역세척은 활성탄의 마모를 일으켜 분탄 누출과 활성탄의 유실을 일으키는 원인이 되기도 한다.

본 실험에서는 공기역세척 2분, 공기+물역세척 30초, 물역세척 5분으로 총 7분 30초간 역세척을 진행하였고, 역세주기는 7~14일 간격으로 실시하였다. Table 6은 역세척한 BAC 여과지에서 5분이 지난 후 BAC 여과수, 후단여과막 처리수의 입자수를 비교한 것이다. BAC 여과수의 2um 이하 입자수와 후단여과막 처리수의 2um 이하 입자수가 약 700배 이상의 차이를 보였다. 후단여과막 처리수의 5um 이하 입자수와 10um 이하 입자수는 측정되지 않은 것을 확인할 수 있다. 이는 후단여과막의 체거름으로 인해 이와 같은 결과가 나온 것으로 판단된다.

3.7. BAC 역세척 후 입자 누출저감 및 안정화 평가

역세척 후 입상활성탄 내부의 부착세균 및 탈리세균, BAC 분탄, 미세플럭 등의 누출에 대한 대책으로 BAC 여과공정 후단에 여과막을 설치하여 BAC 여과수의 안전성을 평가하였다. BAC 역세척 직후 배출, 시동방수시간을 달리하는 배출 그리고 후단여과막을 통과하여 배출하는 3가지 형태로 입자계수 비교를 위한 실험을 수행하였다(Fig. 8).

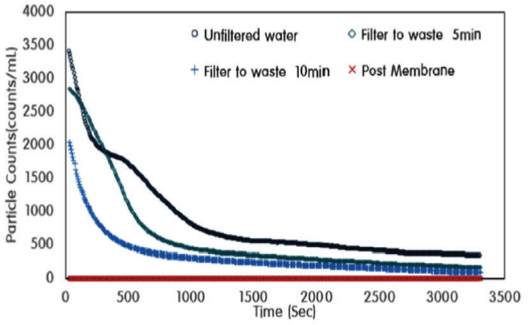


Fig. 8. Comparison of particle counts after backwashing(Ultr–filteredwater/Filter to wate 5, 10min/ Post MF)

역세척 직후 곧바로 배출하였을 경우 최대 입자수가 약 3,500개/mL 정도였으며, 안정기때의 입자수인 20개~30개/mL로 회복되기 위해 걸리는 시간은 5~6시간 정도 소요되었다. 역세척 후 시동방수시간을 달리해서 배출하였을 경우 시동방수시간이 5분일 때 최대 입자수가 3,000개/mL 정도였으며, 안정기의 입자수를 회복하기 위해서는 3시간 정도의 시간이 소요되었다. 그리고 시동방수시간이 10분일 때는 2시간 정도의 시간이 흐른 뒤 입자 수의 안정을 확인할 수 있었다. 반면, 후단막여과공정을 거칠 경우 최대 입자수는 8개/mL 정도로 역세척 전과 후의 차이가 발생하지 않았고, 1분 30초 이내에 안정기 상태인 5개/mL로 회복되었다. 시동방수시간을 길게 할수록 입자수 안정화 시간이 단축되는 것을 확인하였지만, 이로 인해 처리되지 않고 처리공정으로 되돌려지는 물의 양이 상당하게 된다. 하지만 BAC 공정 후단에 여과막 공정을 설치할 경우 되돌려지는 물의 양이 거의 없고, 누출되는 입자가 아주 미미한 것을 확인할 수 있었다.

4_결과 및 고찰

1) 후단여과막을 적용한 경우 기존 고도정수처리와 비교하면 염소소비속도가 25% 감소하고, 염소요구량이 20% 줄어드는 것을 확인할 수 있었다. 또한, 고수온시 (25℃) 기

존 고도정수처리공정보다 염소소비속도는 25.9% 감소하였고, 염소요구량이 16.7% 줄어드는 것을 확인하였다.

2) 고도정수처리공정에서 후단여과막을 적용한 경우 BAC에서 유출된 일반세균은 100%, HPC는 99% 제거하는 것을 확인할 수 있었다.

3) 활성탄 입자가 누출되었을 때, 염소소독 저항성 평가를 위한 실험결과 활성탄이 있는 물을 염소 소독한 경우가 활성탄을 초음파 처리한 후 염소 소독한 경우보다 일반세균수가 높게 나타났는데, 이는 활성탄 입자의 표면이나 갈라진 틈이 미생물의 은신처 역할을 함으로서 염소 소독으로부터 보호되는 것을 확인할 수 있었다.

4) BAC 역세척 전/후의 입자수 안정화 시간을 살펴보았는데, 시동방수 시간이 증가할수록 안정화 시간이 감소하지만, 처리공정으로 되돌료지는 물의 양이 상당하다. 그러나 BAC 공정 후단에 여과막 공정을 설치할 경우 되돌려지는 물의 양이 거의 없고, 누출되는 입자가 아주 미미한 것을 확인할 수 있었다.

연구 결과를 통해서 OBM(Ozone/BAC/Membrane) 공정은 염소요구량 및 염소소비속도가 기존의 O3/BAC 공정보다 20~25% 감소하며, 일반세균과 HPC 그리고 활성탄분탄 등의 입자성 물질 제거에 큰 효과를 미치는 것을 확인할 수 있다. 경제성은 해결해야 하는 부분이나, 향후 멤브레인 시장 확대로 일정 부분 해결할 수 있을 것으로 판단된다. 본 공정에 대한 경제성평가 및 유지관리 가이드라인 수립은 지속적으로 연구되어야 할 것이다.

사사

본 연구는 환경부 "차세대 에코이노베이션 기술개발사업(GT-11-G-02-001-1)"으로 지원받은 과제입니다.

참고문헌

1. 손희종, 유수전, 노재순, 유평종, "정수처리에서의 생물활성탄 공정", 대한환경공학회지 31(4), 308-323 (2009).
2. 백영애, "고도정수처리에서 입상활성탄의 운영 인자 및 재생연구", 서울시립대학교 박사학위논문(2011).
3. LeChevallier, M.W, Hassenaeur, T.S, Camper, A.K, and McFeters, G.A, "Disinfection of bacteria attached to granular activated carbon", Appl Environ Microbiol, Nov 48(5), 918-23(1984).
4. Wang. J. z., Summers, R. S., and Miltner, R. J., "Biofiltration performance : part 1, relationship to biomass", J. Am. Water Works Assoc., 87(12), 55-63 (1995).
5. Scholz, M. and Martin, R., "Ecological equilibrium on biological active carbon," Water Res., 31(12), 2959-22968(1997).
6. Push, A., Losh, D., and Speitel Jr, G. E., "Removal of non-biodegradable chemicals form mixture during granular activated carbon bioregeneration", J. Environ. Eng., 131(2), 196-205(2005).
7. Servais, P., Billen, G., and Bouillot, P., "Biological colonization of granular activated carbon filters in drinking water treatment," J. Environ. Eng., 120(4), 888-899(1994).
8. Chen, W., Waterhoff, P., Leenheer, J. A., and Booksh, K., "Fluorescence Excitation-Emission Matrix Regional Integration to Quantify Spectra for Dissolved Organic Matter," Environ. Sci. Technol., 37(24), 5701-5710(2003).
9. 김현철, "한강원수의 정수과정 중 용존유기물질에 대한 특성 연구," 서울시립대학교 박사학위논문 (2004).
10. Langlais, B., Reckhow, D. A., and Brink, D. R., "Ozone in Water Treatment : Application and Engineering," Lewis Publishers, Inc., Chelsae, Michigan, USA(1991).
11. Giese, A. C., and Christensen, E., "Effects of ozoneon organisms," Physiological Zoology, 27(2) 101-115 (1954).
12. Sproul, O. J., "The mechanism of ozone inactivation of waterborne ciruses", Water Sci. Technol., 14, 303-

314(1982)

13. Ferhan Cecen, Activated Carbon for Water and Waste-water Treatment, Wiley-VCH(2011).

14. 송현우, “고도정수처리공정에서 후단여과막 적용성 연구”, 서울시립대학교 석사학위논문(2015).

Analytical and numerical assessments of local overpressure from hydrogen gas explosions in petrochemical plants

방부형
기술개발팀, 전임연구원
boohyoung.Bang@daewooenc.com

본 논문은 2016년 Fire and Materials의 Online Library에 게재되었던 논문을 재게재한 것입니다.

Abstract

Accurate prediction of pressure rise is important for safety assessments of a petrochemical plant in the event of an explosion accident. The sudden pressures arising from gas explosions at various hydrogen concentrations in air have been predicted analytically and numerically. These solutions were compared against experimental data. The analytical solution, based on the self-similar solution for pointwise strong explosions in an open space, which assumed no energy loss and premixed fuel-air mixture, reasonably predicted the explosive-ignition detonation case while the numerical solutions were more suitable to model spark ignition deflagration cases that accounted for the effect of turbulence arising from three-dimensionality and presence of obstacles in the computational domain. Comparison of both analytical and numerical results against experimental data indicates that their differences are within a 30% margin. The analytical model presented herein can be useful for field engineers who want conservative estimates of the overpressure resulting from explosive-ignition detonation.

Keywords : petrochemical plant; gas explosion; overpressure; analytical solution

1_INTRODUCTION

In petrochemical plants, unexpected releases of combustible vapors/gases can lead to explosions, which threaten the integrity of equipment and structures. Multiple explosions can destroy plants, jeopardize lives, and inflict large economic losses; outdated parts of the pipe system can leak flammable gas in air and pose the danger of explosion as illustrated in Figure 1 [1, 2]. Therefore, it is important to be able to predict explosion properties and to design pipes and storage tanks that can withstand such catastrophic events. Such efforts enable plant engineers to evaluate risks associated with their designs subject to various possible explosions. Pressure rises almost instantaneously because of the overpressure from an explosion causing structural damage or deformation of pipes and storage tanks. Explosive pressure and structural damage can be estimated with analytical and numerical tools. By using these computational tools, safe distances between equipment and structures can be assigned.

It is easy to envision how a flammable vapor could leak into an unconfined/open area of a plant. If the leaked fuel concentration in air is low and the vapor cloud is diluted, explosion is unlikely to occur, especially if unobstructed and far from nearby structures. However, one must consider the worst-case accident scenario; case in point is a large mass of a flammable gas in the scale up to a few hundred kg well mixed in air in stoichiometric ratio in a confined space. This amount of leakage of the flammable gas may

arise when safety alert systems fail during an unexpected circumstance such as a terrorist attack. In this worst-case scenario, flame velocity is high, and deflagration almost immediately changes to detonation, resulting almost instantaneously in a powerful explosion and formation of a shock wave propagating in air. The evaluation of the worst-case accident scenario should be accounted for when structural designs are developed. This is needed for a conservative estimate of the safety-related issues associated with design of equipment and structures so that they can withstand such a harsh explosive environment.

Explosive pressure can depend on several factors, such as fuel type, fuel mass, the fuel–air ratio, location of the ignition point, the ignition-source strength, the presence of surrounding obstructions, shock wave propagation, turbulence developing in air, and ambient winds. Most aspects can be taken into account using a computational fluid dynamics code, such as FLame ACceleration Simulator (FLACS), which simulates a release of gas and its subsequent explosion. FLACS has been preferred by plant engineers for its long history of reliable use in both onshore and offshore applications.

Although FLACS is a powerful computational tool that simulates gaseous explosions, it cannot simulate detonation phenomena, in particular, the explosive ignition (or strong explosion) case, for which the analytic self-similar solution should be used. The classical theory of strong explosions implies an instantaneous, pointwise release of the explosion energy and thus allows for an analytical solution for the gas dynamics of the resulting gas flow [7–13]. In particular, it predicts the pressure, gas velocity, and density at the shock wave front. For this reason, the capability of FLACS and theanalytic self-similar solution in predicting the overpressure for deflagration and detonation cases, respectively, has been evaluated in this work.

The experimental data on hydrogen concentration and ignition type of hydrogen–air mixtures in an open space will be used for comparison. A quiescent, homogenous mixtures of 20% to 30% hydrogen by volume filling 5.2 and 37-m3 tents were employed in the experiments of [14]. In these experiments, a stoichiometric (30%) and lean (20%) hydrogen–air mixtures were ignited by a spark, which produced deflagration. When ignited by an explosive, the flame was categorized as ‘detonation’. Further details on the experiment are available in Section 3.1. In Section 3.2, the FLACS prediction of the overpressure at varying hydrogen mass has been presented.

2_MODELING DESCRIPTION

2.1. Numerical Simulation of Weak Explosions by FLACS

In general, the pressure rise and the resulting overpressure are expected to be estimated from both computational and experimental

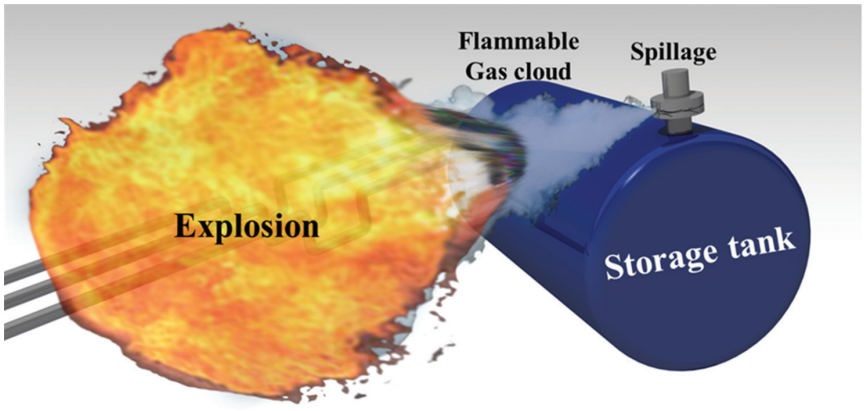


Fig. 1. Schematic of an explosion and its effects.

studies because these parameters determine structural damage. For a fuel vapor-cloud explosion at a petrochemical plant, which occupies a significant space and thus are dilute, devastating supersonic detonation is not anticipated, and in such unconfined/open area clouds overpressures do not exceed a few bar. This relatively weak explosion case is considered deflagration. The flame front, as is well known, generates turbulence, as well as the surrounding obstacles, thereby increasing the burning rate. This, in turn, results in fast deflagration wave/flame propagation further increasing turbulence.

2.1.1 Governing Equations

The governing equations used in FLACS include the mass (1), momentum (2), enthalpy balances (3), the turbulent kinetic energy balance (5), and the equation (6) for dissipation rate of turbulent kinetic energy as introduced in Ref. ("FLACS User's Manual 10.2", 2014). The size of the computational domain was 200 200 100 m^3, which replicated the actual plant including a gas central processing unit and other additional facilities. A total number of the two millions computational nodes were used. The CFL number of 0.5 was used to secure numerical stability. The simulation duration was limited to 1 s.

$$\frac{\partial \rho}{\partial t}(\beta_v \rho) + \frac{\partial}{\partial x_j}(\beta_j \rho u_j) = \frac{\dot{m}}{V} \quad (1)$$

$$\frac{\partial}{\partial t}(\beta_v \rho u_i) + \frac{\partial}{\partial x_j}(\beta_j \rho u_i u_j) = -\beta_v \frac{\partial P}{\partial x_i} + \frac{\partial}{\partial x_j}(\beta_j \sigma_{ij}) + F_{o,i} + \beta_v F_{w,i} + \beta_v(\rho - \rho_0) g_i \quad (2)$$

$$\frac{\partial}{\partial t}(\beta_v \rho h) + \frac{\partial}{\partial x_j}(\beta_j \rho h u_j) = \frac{\partial}{\partial x_j}\left[\beta_j \frac{\mu_{eff}}{\sigma_h}\frac{\partial h}{\partial x_j}\right] + \beta_v \frac{DP}{Dt} + \frac{\dot{Q}}{V} \quad (3)$$

$$\frac{\partial}{\partial t}(\beta_v \rho \Upsilon_{fuel}) + \frac{\partial}{\partial x_j}(\beta_j \rho u_j k) = \frac{\partial}{\partial x_j}\left[\beta_j \frac{\mu_{eff}}{\sigma_{fuel}}\frac{\partial \Upsilon_{fuel}}{\partial x_j}\right] + R_{fuel} \quad (4)$$

$$\frac{\partial}{\partial t}(\beta_v \rho k) + \frac{\partial}{\partial x_j}(\beta_j \rho u_j k) = \frac{\partial}{\partial x_j}\left[\beta_j \frac{\mu_{eff}}{\sigma_k}\frac{\partial k}{\partial x_j}\right] + \beta_v P_k - \beta_v \rho \varepsilon \quad (5)$$

$$\frac{\partial}{\partial t}(\beta_v \rho \varepsilon) + \frac{\partial}{\partial x_j}(\beta_j \rho u_j \varepsilon) = \frac{\partial}{\partial x_j}\left[\beta_j \frac{\mu_{eff}}{\sigma_\varepsilon}\frac{\partial \varepsilon}{\partial x_j}\right] + \beta_v P_\varepsilon - C_{2\varepsilon}\beta_v \rho \frac{\varepsilon^2}{k} \quad (6)$$

Constants required for the k- turbulence model are taken from Ref. (Launder & Spalding, 1974). The compressible 3D Navier-Stokes equations are solved by using a finite-volume method in FLACS. Ref. (Hjertager, 1984, 1986) describe the implementaton of the basic equations and Ref. (Hjertager, Fuhre, & Bjrkhaug, 1988) presents the experimental data of explosion to validate FLACS. FLACS uses a 2nd order scheme for resolving diffusive terms and a 2nd order hybrid scheme to resolve convective terms. The time marching steps is advanced by a 1st order backward Euler scheme to secure numerical stability. The SIMPLE pressure-correction algorithm (Patankar, 1980) is applied and modified to extend its scheme to compressible flows with extra source terms which accounts for the work term by compression in the enthalpy equation. Iterations are applied until residuals is less than a certain tolerance.

When a combustible cloud is ignited close to the quiescent conditions, the initial burning process is laminar. The flame front is smooth and flame propagation is entirely governed by thermal and/or molecular diffusion processes (YaB, Barenblatt, Librovich, & MakhviladzeZeldovich et al., 1985). Shortly after this stage, instabilities originating from various sources (e.g., ignition, flow dynamics, the Rayleigh-Taylor instability) warp the flame surface resulting in an increased, quasi-laminar flame speed. Depending on the flow conditions, the deflagration front can accelerate and create a shock wave, which is sustained by the exothermic chemical reaction behind its front, i.e. deflagration wave can transform itself into a detonation wave. Such a transition can happen in the turbulent burning regime. The laminar burning-velocity depends on the type of fuel, fuel-air mixture, and pressure. The laminar burning velocities at different equivalence ratios are tabulated for various fuels and the laminar burning velocity of a fuel mixture is calculated as the volume-weighted average. In the quasi-laminar regime, the turbulent burning velocity is computed. Then the turbulent burning velocity is a simplified form of the expression available in Ref. (Bray, 1990), where the Karlovitz stretch factor including the turbulent Reynolds number is used.

2.1.2 Combustion Models

Ignition is initiated when flammable gas concentration is sufficiently high. Once ignited, laminar burning velocity is calculated associated with chemical reactions of combustion. The turbuence model (turbulent burning velocity) is triggered by the Rayleigh-Taylor instability at the flame-air interface and associated with the flow field and wall shear stresses, buoyancy, sub-grid object models, etc.

Ignition of a premixed cloud of fuel and oxidant may escalate to an explosion, but before that the laminar burning velocity is:

$$S_L^0 = S_L^0(\text{fuel}, \Phi), \tag{7}$$

which depends on the fuel and the equivalence ratio. For mixtures with fuel contents outside of the lower and upper flammability limits, the laminar burning velocity is zero (they will not burn). In an explosion, the flame accelerates and becomes turbulent with a significantly higher burning velocity due to improved mixing of reactants and products. FLACS uses correlations for both laminar and turbulent burning velocities derived from experimental work.

Because the reaction zone in a premixed flame is thin compared to the grid resolution, the flame zone is thickened by increasing the diffusion and reducing the reaction rate by factors of (the - model).

2.1.3 Flame Model

The diffusion coefficient in the transport equation for fuel is:

$$D = \frac{\mu_{eff}}{\sigma_{\text{fuel}}}. \tag{8}$$

In the - model, the dimensionless reaction rate, W, and diffusion coefficient are adjusted as:

$$W^* = \frac{W}{\beta} = W\frac{l_{LT}}{\Delta_g}, \tag{9}$$

$$D^* = D\beta = D\frac{\Delta_g}{l_{LT}}. \tag{10}$$

2.2. Analytical Simulation of Strong Explosions

After escape of a flammable gas it mixes with the surrounding air yielding a premixed flame explosion scenario. Once the fuel-air cloud explodes/ignites instantaneously on a large scale, a shock wave propagates in the surrounding gas. Pressure and temperature behind the shock wave front are high, and the if the chemical reaction at its front could continue, it can create a self-sustaining detonation wave. A sonic or supersonic detonation wave is sustained by the combustion reactions at the shock wave front and propagates into an unburned gas at speeds of 1,500 to 2,000 m/s resulting in overpressures in the 15 to 20 bar range. The classical theory of strong explosions, however, implies that the chemical reaction is over instantaneously (at the moment of strong explosion) and deals with propagation of the shock wave alone. The theory of strong explosions specifies, among other parameters, the pressure, P_{sh}, gas velocity, V_{sh}, and density, $_{sh}$, at the shock wave front as in Refs. (Lifshitz & Landau & Lifshitz, 1987; Sedov, 1946, 1993; Taylor, 1950a, 1950b; von Neumann, 1963; Yarin, 2007):

The strong-explosion theory is based on the assumption that the explosion energy, E_0, is released instantaneously at a point. This implies that fuel is instantaneously evaporated and mixed with the oxidizer, and the reacting mixture is stoichiometric. The theory also neglects energy losses due to thermal radiation all energy is preserved. These assumptions tend to overestimate the strength of the shock wave. In reality, liquid methane spillage and evaporation, for example, will take some time and space, and are accompanied by liquid atomization (losses). Also, mixing with the oxidizer (oxygen in air) can be far from complete when the explosion occurs, and nitrogen in air will act as a thermal ballast. Typically, a fuel-oxidizer mixture will not be fully pre-mixed. These factors diminish the strength of a real shock wave compared to these ideal predictions. The strong-explosion theory is purely gas dynamical and does not consider turbulent eddy viscosity and the effect of turbulence on the energy-release rate. As it stated before, the strong-explosion theory does not imply formation of a self-sustaining detonation wave, since the chemical reaction is assumed to be over instantaneously. With all the simplifying assumptions listed above, the first estimates of the strong explosion effects

should be based on the strong-explosion theory outlined above.

3_RESULTS AND DISCUSSION

Table 1 summarizes the case studies we have conducted herein. Because Cases A and B are deflagrations, these experimental data are compared to FLACS simulations. Because the analytical solution was obtained for an almost instantaneous explosion reminiscent of detonation, it is compared to Case C. Cases 1 and 2 reflect small and large volumes corresponding to 5.2 and 37 m^3 of the hydrogen/air mixture in a confined plastic tent, respectively.

Table 1. Case studies compared to experimental results

Calculation	FLACS		Eq.(24)
Ignition type	Spark (deflagration)		Explosive (detonation)
Hydrogen concentration (Mixture type)	A (Lean)	B (Stoichiometric)	C (Stoichiometric)
Case 1 (5.2 m^3)	20%	30%	30%
Case 2 (37 m^3)	20%	30%	30%

In the experiment, overpressure was recorded using PCB Piezotronics model 133A36, 137A23, and 112M343 quartz pressure transducers, which were installed at increasing distances from the ignition source. Pressure measurements at R reflect blast-wave travel times. The blast wave travels subsonically and supersonically for deflagration or detonation, respectively. Both deflagration (Cases A and B) and detonation (Case C) ignitions are considered; Cases A and B were ignited by a spark and Case C was ignited by an explosive. The spark was generated with a 40-J capacitive discharge unit while a 10 g booster of C-4 explosive (5.210^4 J) was used to detonate the stoichiometric mixture with 30% hydrogen volume. Masses of 20% hydrogen by volume are considered lean while 30% hydrogen by volume is considered stoichiometric when mixed with air. The mixtures are assumed homogenous and quiescent.

Figure 2a compares the numerical results from FLACS to the experimental data of Ref. (Sato et al., 2006) for Case A, which is a lean deflagration case. The x-axis indicates the distance away from the ignition point, normalized by the characteristic length defined as R0 = $(E_0/P_0)^{1/3}$, where E_0 is the combustion energy (LHV) of hydrogen, and P_0 is atmospheric pressure. This dimensionless parameter is known as the Sachs-scaling distance, which is a common standard (Sachs, 1944). Their curvatures in overpressure appear to be consistent, but their absolute overpressure values moderately differ, except the starting and end points. The FLACS simulation appears to under-predict the experimental results in case of the lean combustion case. However, as for the stoichiometric case B, their difference is greatly reduced; see Figure 2b. The FLACS simulation still under-predicts the experimental data, however, the prediction is much closer to the experimental data, as compared to the lean combustion case A.

FLACS has not been incorporated with the subtle difference in the ignition energy. FLACS simply assumes ignition is initiated when flammable gas concentration is higher than a certain threshold which is in general set by a software user. FLACS assumes ignition of a premixed cloud of fuel and oxidant. When this concentration of premixed cloud is low (such as Cases A), the degree of the explosion of this lean combustion case in FLACS cannot be up to the level of the real (or experimental) combustion, which is the shortcoming of FLACS. However, when the concentration of the premixed cloud is high (such as Case B), the comparison between FLACS predictions and experimental data has improved significantly; see Figure 2b. This excellent agreement indicates FLACS accurately predicts the overpressures resulting from deflagration when the fuel-air concentration is relatively high. In addition, it should be reminded that FLACS semi-empirically accounted for the effect of the generated turbulent eddies on the flame propagation, as well as the detailed kinetics of the combustion reaction, which in turn helps the model to realistically match the experimental data.

In Figure 2c, the detonation case C has been studied by comparing the analytic predictions for a shock wave produced by a strong explosion against the experimental data. The comparison shows good agreement. There are two reasons for that. First, the analytic

self-similar solution corresponds to a pointwise strong explosion in an open spherical space, which is very close to the experimental case C. Second, it stems from the fact that the chemical reaction behind the shock wave front rapidly expires, and a pure shock wave rather than a detonation wave arises, even though the real explosion was not exactly instantaneous.

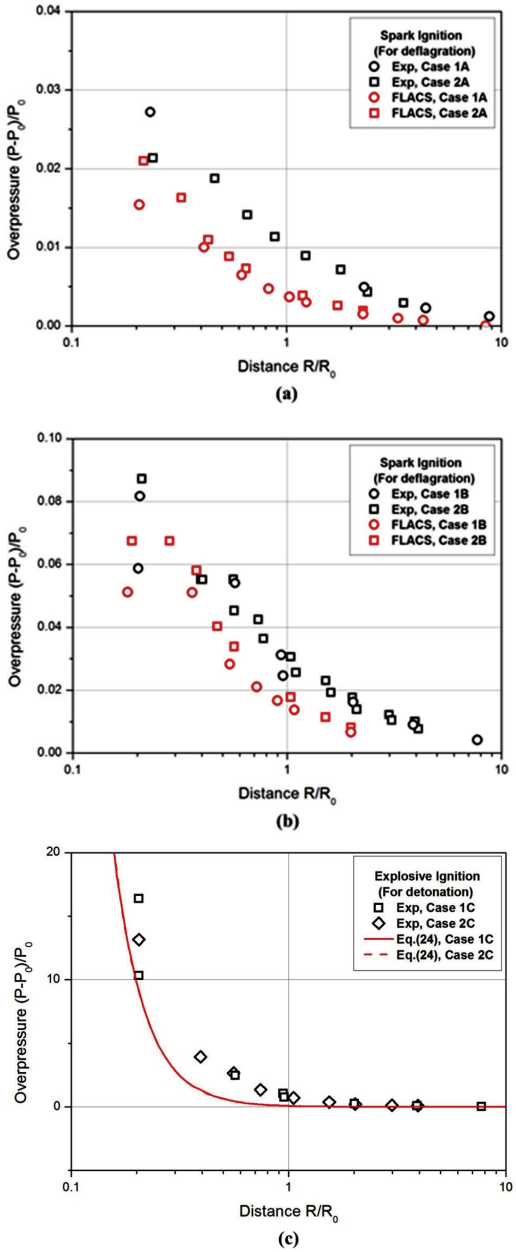


Fig. 2. Simulated overpressures compared to experimental data. (a) Case A: Spark ignition (deflagration) lean mixture type, (b) Case B: Spark ignition (deflagration) stoichiometric mixture type, (c) Case C: Explosive ignition (detonation) stoichiometric mixture type

As shown in Figure 2a and b, the experimental overpressure data are relatively insensitive to the total volume of hydrogen as there are no discernable difference between Cases 1 and 2 regardless of whether the ignition was by spark or detonation. However, FLACS simulations indicate differences between Cases 1 and 2. Overpressure from the large volume (37 m^3, solid curves) is greater than overpressures from the small volume 5.2 m^3, dashed curves) because more hydrogen yields a more powerful blast wave.

Figure 3 quantifies the deviation of the simulations from the data at R/R_0 0.4, which appears to be satisfactory, considering the uncertainties associated with both numerical predictions and experimental data.

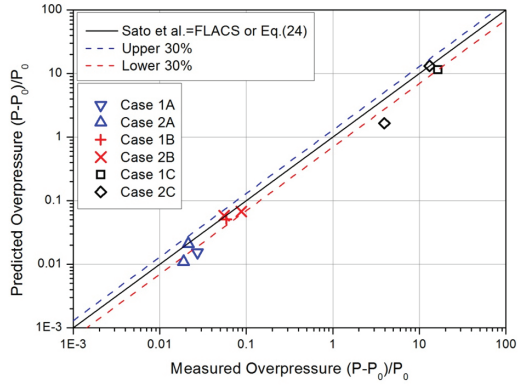


Fig. 3. Cross plot of CFD and the analytical theory for overpressure estimates.

4_CONCLUSIONS

Overpressure due to hydrogen explosions was estimated using the 3D computational code (FLACS) and the analytic solution based on the theory of strong explosion. These estimations were compared against the existing experimental data. The analytic solution was found to be appropriate to model the detonation case, where the chemical reaction behind the shock wave front

rapidly fades and the later deteriorates to a pure shock wave, while FLACS was more appropriate to model the deflagration cases. The 3D numerical results accounted for the effect of the generated turbulent eddies on the flame propagation and the kinetics of the combustion reaction while the analytic solution did not consider these effects and concentrated on the shock wave propagation in the gas dynamical limit. This indicates that the turbulent eddies and the detailed kinetics effects were significant to affect the overall overpressure during deflagration. On the other hand, during detonation, the initial explosive energy of hydrogen released almost instantaneously was the most dominant factor that affected the overpressure. We found that the overpressure did not exceed the value of 1 bar for the hydrogen mass of <400 kg. The overpressure of less than 1 bar quickly dissipated and was equalized with the surrounding atmospheric pressure within a second; thus, the nearby surrounding structures will highly unlikely be damaged in this overpressure range.

REFERENCES

1. Arntzen, B.J. (1998). Modelling of turbulence and combustion for simulation of gas explosions in complex geometries.
2. Baker, W.E., Cox, P.A., Kulesz, J.J., Strehlow, R.A., & Westine, P.S. (2012). Explosion Hazards and Evaluation: Elsevier, Amsterdam.
3. Bang, B., Park, H.-S., Kim, J.-H., Al-Deyab, S.S., Yarin, A.L., Yoon, S.S. (2016).
4. Simplified method for estimating the effect of a hydrogen explosion on a nearby pipeline. Journal of Loss Prevention in the Process Industries, 40, 112-116.
5. Bray, K.N.C. (1990). Studies of the turbulent burning velocity. Proceedings of the Royal Society of London. Series A: Mathematical and Physical Sciences, 431(1882), 315-335.
6. Davis, S.G., Engel, D., Gavelli, F., Hinze, P., & Hansen, O.R. (2014). Advanced Methods for Determining the Origin of Vapor Cloud Explosions Case Study: The 2006 Danvers Explosion Investigation. Fire Technology, 50(4), 823-850.
7. FLACS User's Manual 10.2. (2014). from GexCon AS
8. Garcia, J., Baraldi, D., Gallego, E., Beccantini, A., Crespo, A., Hansen, O.R., Yanez, J. (2010). An intercomparison exercise on the capabilities of CFD models to reproduce a large-scale hydrogen deflagration in open atmosphere. International Journal of Hydrogen Energy, 35(9), 4435-4444.
9. Hjertager, B.H. (1984). Computer simulation of turbulent reactive gas dynamics.
10. Hjertager, B.H. (1986). Three-dimensional modeling of flow, heat transfer, and combustion. Handbook of Heat and Mass Transfer, 1, 1303-1350.
11. Hjertager, B.H., Fuhre, K., & Bjørkhaug, M. (1988). Gas explosion experiments in 1: 33 and 1: 5 scale offshore separator and compressor modules using stoichiometric homogeneous fuel/air clouds. Journal of Loss Prevention in the Process Industries, 1(4), 197-205.
12. Kletz, T. (2009). What Went Wrong?: Case Histories of Process Plant Disasters and How They Could Have Been Avoided: Butterworth-Heinemann.
13. Launder, B.E., & Spalding, D.B. (1974). The numerical computation of turbulent flows. Computer methods in applied mechanics and engineering, 3(2), 269-289.
14. Landau, L.D. & Lifshitz, E.M., (1987). Fluid Mechanics. Volume 6 (Course of Theoretical Physics) Butter-worth -Heinemann.
15. MARSH (2014). The 100 Largest Losses (in the Hydrocarbon Industry) 1974-2013.
16. Middha, P., & Hansen, O.R. (2009). Using computational fluid dynamics as a tool for hydrogen safety studies. Journal of Loss Prevention in the Process Industries, 22(3), 295-302.
17. Molkov, V.V., Makarov, D.V., & Schneider, H. (2007). Hydrogen-air deflagrations in open atmosphere: large eddy simulation analysis of experimental data. International Journal of Hydrogen Energy, 32(13), 2198-2205.
18. Patankar, S. (1980). Numerical Heat Transfer and Fluid Flow: CRC Press. Boca Raton.
19. Sachs, R.G. (1944). The dependence of blast on ambient pressure and temperature: DTIC Document.

20. Sato, Y., Iwabuchi, H., Groethe, M., Merilo, E., & Chiba, S. (2006). Experiments on hydrogen deflagration. Journal of Power Sources, 159(1), 144-148.
21. Sedov, L.I. (1946). Propagation of strong blast waves. Journal of Applied Mathematics and Mechanics, 10, 241 - 250.
22. Sedov, L.I. (1993). Similarity and Dimensional Methods in Mechanics: CRC Press. Boca Raton.
23. Taylor, G. (1950a). The formation of a blast wave by a very intense explosion. I. Theoretical discussion. Proceedings of the Royal Society of London. Series A, Mathematical and Physical Sciences, 159-174.
24. Taylor, G. (1950b). The formation of a blast wave by a very intense explosion. II. The atomic explosion of 1945. Proceedings of the Royal Society of London. Series A, Mathematical and Physical Sciences, 175-186.
25. von Neumann, J. (1963). The point source solution (Collected Works, Vol. VI): Pergamon Press.
26. Zeldovich, Ya. B., Barenblatt, G.I., Librovich, V.B., & Makhviladze, G.M. (1985). The Mathematical Theory of Combustion and Explosions. Consultants Bureau, New York.
27. Yarin, A.L. (2007). Self-similarity, Chapter 2.3 in Springer Handbook of Experimental Fluid Mechanics: Springer. Heidelberg.

Method for Installation of Marine HDPE Pipeline

Youngtae Kim
Technology Development Team
youngtae.kim@daewooenc.com

K.S. Park
Steel Business Division, POSCO Center,
Seoul Republic of Korea

A.S. Choi
Braduate School & Engineering Mastership,
POSTECH, public of Korea

S.Y. Yu & D.K. Kim
Department & Civil and Environmental Engineering,
Universiti Teknolog PETRONAS, Malaysia

본 논문은 ICCOEE (International Conference on Civil, Offshore & Environmental Engineering) 2016에 발표된 내용이며, 도서 Engineering Challenges for Sustainable Future pp. 113~118 에 게재된 논문을 재게재한 것입니다.

Abstract

A seawater intake system of a power plant has the function of transferring cooling water to condenser and auxiliaries. An HDPE pipeline in the marine environment has been used for seawater intake system due to its advantages such as immunity to galvanic corrosion, light weight and flexibility. In order to use the HDPE pipeline safely, sinking analysis and rigorous study should be performed. Daewoo Engineering and Construction Ltd. has successfully installed an ultra-diameter of 2500mm HDPE pipeline for Ras Djinet Combined Cycle Power Plant in Algeria. This paper will introduce the design and analysis for installation of HDPE pipeline.

Keywords : HDPE, Pipeline, Installation, Design

1_INTRODUCTION

A power plant has a seawater intake system to deliver cooling water to condenser and auxiliaries. It consists of a cooling water (C.W.) intake head structure, C.W. intake pipeline, and intake basin structure. Recently, Daewoo Engineering and Construction (Daewoo E&C) has successfully constructed the intake pipeline system for the Ras Djinet Combined Cycle Power Plant project in Algeria. Various type of pipeline material for the intake structure has been used such as steel pipeline, Glass Reinforced Epoxy (GRE), and High-Density Polyethylene (HDPE) materials. This project adopted HDPE materials considering benefits of immunity to galvanic corrosion, light weight, and flexibility.

HDPE pipeline has become an attractive alternative in oil and gas industry because of its strength, durability, light weight, and its joint-less construction method (Rinker Pipeline Systems, 2004). Thus, it is suitable for marine application such as subsea pipeline (Idris, 2008). HDPE pipeline needs concrete ballast units to be placed on the seabed which is to withstand buoyancy force and lateral hydrodynamic force. Corrugated HDPE generally has a minimum design service life of 50 years. (Kang et al. 2009). Corrugated HDPE also has a vertical deflection of the central soil prism greater than adjacent backfill soil prisms. It causes a positive arching action and resulting in a vertical arching factor (VAF) less than one. Corrugated HDPE is more sensitively affected by the interface condition where vertical load induced due to shearing stress than the radial pressure (Kang et al. 2009).

In addition, HDPE is also widely used for lining system which is used in pipeline to enhance corrosion resistance as well as to line damaged pipeline. However, polymer liners can fail in service as well. It could be due to buckling collapse induced by external pressure as well as the aging problem. Failure mode due to buck-

ling collapse induced by external pressure is caused by the combined action of two separate factors such as rapid decompression of pipeline and the permeation of oil derived gasses through the liner wall (Rueda et al. 2015). The rapid decompression of pipeline usually happens during service maintenance and inspection shutdowns. Several analytical models were proposed regarding the buckling collapse of pipeline induced by external pressure (Jacobsen 1974, Glock 1997, El-Sawy 2001).

However, it is worth to note that the analytical models are only applied to purely elastic or ideal elastoplastic behavior. They are unable to describe the behavior of highly strain-rate and time-dependent materials as well as the whole deformation process. To overcome the limitation of these analytical models, an FEM model for the simulation of the buckling collapse of HDPE liners was developed by Rueda et al (2011). Other than using FEM model to simulate the buckling collapse of polymetric pipeline, there are also several methods proposed by Boyce at al. (1988), and Bergstrom et al. (2004; 2010).

Aging problem is also one of the main factors that cause failure of pipe liners. Numbers of previous studies have been done in this field for different types of polymers in terms of aging temperature effect (Mohd Ishak et al. 2000; Pegoretti and Migliaresi 2002; Chen et al 2007; Guermazi et al. 2009). The outcome shows that the degradation process of pipeline liner is obviously affected by aging problem.

This study focuses on subsea pipeline installation using HDPE. Song et al. (2015) performed an installation analysis on HDPE pipeline to analyze the structural stability during installation. The purpose of this study is to find a general trend and design consideration throughout the parametric study. To perform installation analysis of the HDPE pipeline, below information is applied. The sea water intake pipeline are approximately 1.0 km and consist of four (4) lines with 2,500 mm outer diameter (OD) HDPE pipeline.

2_DESIGN OF HDPE PIPELINE

The basic design for marine HDPE pipeline system is performed as follows:

2.1. Selection of pipeline diameter

Pipeline diameter is required to estimate the minimum flow in order to achieve the suitable flow rate which is designed to meet cooling system criteria. The intake system for the project is designed to intake seawater of 162,360 m^3 per hour and diameter was selected to 2500 mm accordingly to meet the limit flow velocity.

2.2. Selection of pipeline wall thickness

In order to select reliable wall thickness of pipeline, core resistant factor to cover internal pressure and external load is considered. Several criteria should be met to determine the pipeline wall thickness. They are as follows:

- Bursting criteria under internal pressure
- Pipeline ring deflection under hydrostatic pressure
- Combined stress under burial load and buckling criteria under installation load.

The wall thickness of SDR 30 and 26 pipelines are confirmed to have the most required thickness based on the pressure containment calculation.

Selection of required weight and spacing of ballast weight for concrete collar.

The submerged weight of pipeline should be calculated considering both cases of empty and flooded pipeline. The empty condition makes pipeline float in the water surface i.e., the pipeline is neither sinks nor floats.

Pipeline laid on the seabed will be exposed to marine environments such as current and wave before backfilling. 2-year significant wave height and current conditions are considered to design required weighting and spacing for its stability against marine environment due to a temporary condition.

On-bottom stability was performed to check the stability of the pipeline on the seabed. Pipeline resting on the seabed are significantly subjected to the forces due to wave and current loads. If

a pipeline is not stable then it will move to the actions of waves and currents. In order to meet the criteria for on-bottom stability and required submerged weight to sink the pipeline, the concrete collar volume is designed to 6.7 m3 with 6m span which is equivalent to 135 mm of concrete coating thickness along the pipeline. Thespanlengthof the concrete collar then checked to meet the criteria free-span length considering static and dynamic condition. Concrete collars inevitably make gaps between pipeline and seabed and its span is the length of concrete collars as shown in Fig. 1.

As a result from the stability analysis, a weighting of 40 % should give proper stability on a pipeline laid on a flat seabed. The trench effect would compensate the force with sheltering effect from trench estimating to 20%. A net weighting of 32 % of the weight of sea water displaced by the pipeline, 5.03 t/m was proposed. The pipeline with this weighting would resist against wave and current before backfilling (Ian Larsen 2013).

Table 1. HDPE pipeline key design characteristics

Description		Intake Pipeline A	Intake Pipeline B
Type	–	SDR30	SDR26
Material	–	HDPE	HDPE
Material Grade	–	PE100	PE100
Pipeline Outer Diameter	mm	2500	2500
Service	–	Raw Sea Water	Raw Sea Water
Pressure Regime	–	LP	LP
WallThickness	mm	83.3	96.2
Design Pressure	bar(g)	5.5	6.4
Design Temperature	℃	40	40
Operating Temperature	℃	24	24
Minimum Required Strength (MRS)	MPa	10	10

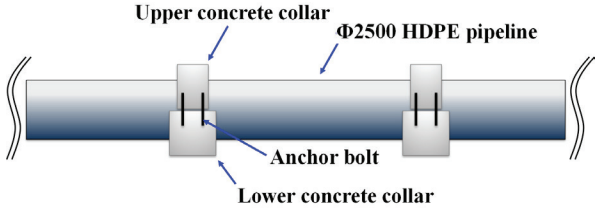


Fig. 1. Schematic of HDPE pipeline with concrete collar (Kim, 2015)

3_INSTALLATION ANALYSIS OF HDPE

Installation analysis for sinking pipeline floated on the surface should be performed according to the pipeline basic design. This analysis will determine the maximum von-Mises stress, bending radius and curvature during pipeline sinking. Table 1 and Table 2 show the key characteristics of the designed HDPE pipeline and material properties.

The designed concrete collar to give ballast during sinking was finally constructed as shown in Fig. 2.

The commercial software Orcaflex 9.6 was used to perform the sinking analysis. Orcaflex is a marine dynamic program developed by Orcina for static and dynamic analysis of a wide range of offshore systems including all types of marine risers (rigid and flexible), global analysis, moorings, installation and towed systems.

Table 2. High–density polyethylene properties for HDPE100

Property	Unit	Value
Density	kg/m^3	960
Tensile Yield Strength	MPa	23
Elongation at Yield	%	8
Tensile Break Strength	MPa	37
Coefficient of Thermal Expansion	m/m/℃	2.4x10^{-4}
Poisson's Ratio	–	0.4
Minimum Required Strength at 23℃(MRS)	MPa	10.0
Hydrostatic Design Stress at 23℃(MRS)	MPa	7.7



Fig. 2. Pre-cast concrete collar

The following results are extracted from the sinking analysis:

- Minimum bending radius (or pipeline curvature) along the pipeline
- Maximum von-Mises stress in the pipeline Based on the results of the analysis, the following pertinent information required for the sinking installation will be obtained:
- Tension capacity required from the tensioning tug and the recommended pulling tensions
- Stress during various stages of flooding/sinking operation

As Orcaflex is not able to simulate the pipeline content change from empty to flooded condition, the pipeline was modeled that the pipeline initially flooded during floating out but additional buoyancy tanks are attached to compensate the initially flooded water weight inside the pipeline. Subsequently, releasing the tank one by one from the offshore end is performed to simulate the flooding process, so that the pipeline could be laid down on the seabed.

The configurations and sinking of the offshore and pipeline sections are illustrated in Fig. 3.

To prevent buckling failure, the minimum bending radius shall be maintained during pipeline installation. The minimum short-term bending radius shall be as follows (AWWA 2013):

- Pipeline dimension ratio range 13.5 – 21 in: 17 times pipeline OD
- Pipeline dimension ratio larger than 21 in: 20 times pipeline OD

This criterion was checked in the pipeline installation analysis. The analysis was performed considering that the crane is positioned at 60 meters offshore from the inshore end of the pipeline to lift the pipeline floated from the water surface. This is to ensure that initial water flooding starts and begins at the inmost end of the inshore pipeline.

The pulling force at the offshore end was analyzed to figure out the effect of pulling force on the bend radius and von-Mises stress. The results show that the pulling force of above 50 ton meets the criteria for the minimum bending radius and von-Mises stress as shown Fig. 4. But the pulling force of above 60 ton would give margin for the safety of 1.5 as the value of 75 m, i.e. 30-time pipeline OD.

During installation in the field, the way of pipeline being charged

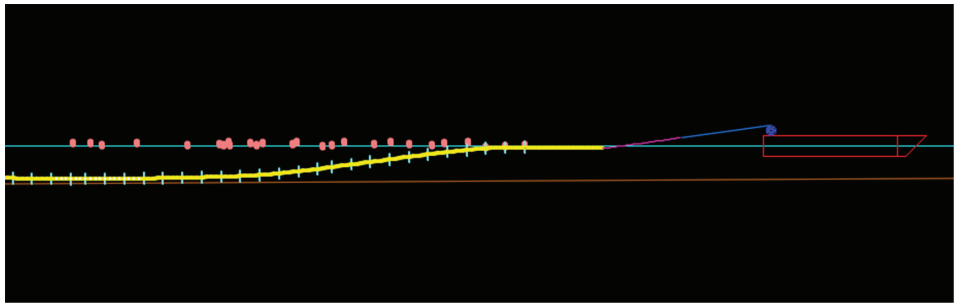
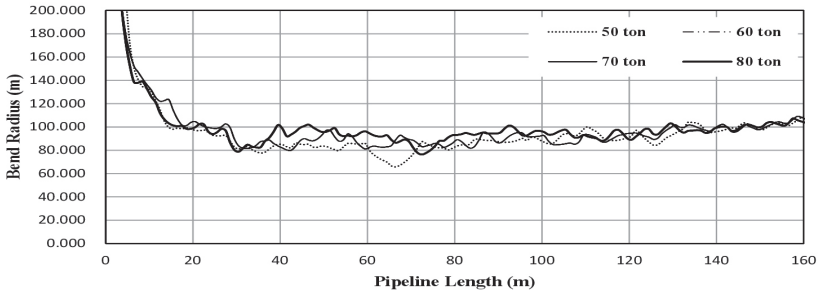
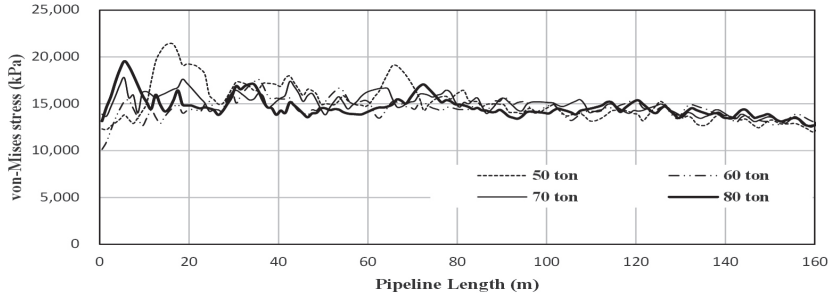


Fig. 3. Orcaflex modeling for HDPE pipeline sinking analysis.

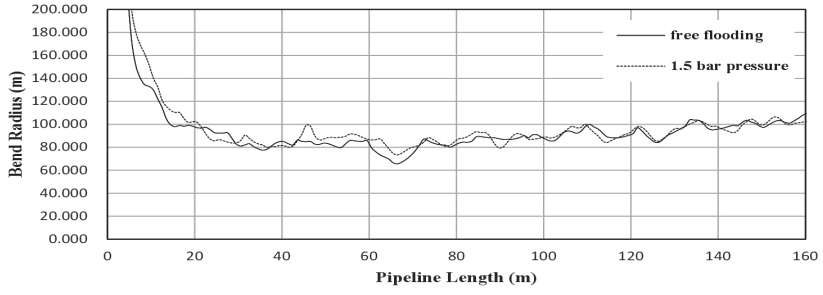


(a) Bend radius corresponding to the different pulling force

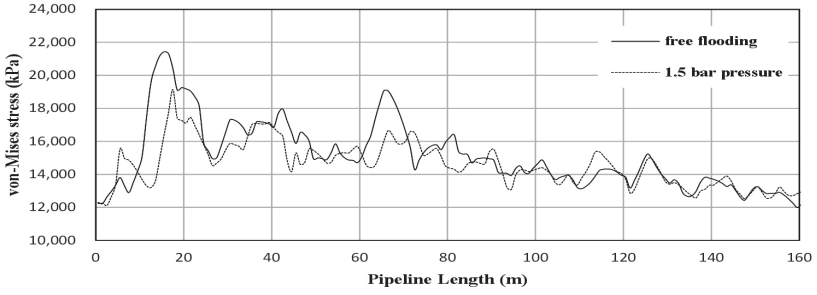


(b) von–Mises stress corresponding to the different pulling force

Fig. 4. Effect of pulling force.



(a) Bend radius in case of free flooding and 1.5 bar compressed air



(b) von–Mises stress in case of free flooding and 1.5 bar compressed air

Fig. 5. Effect of internal pressure with pulling force 50 ton.

with compressed air at 1.5 bar was applied to reduce the stress in the pipeline. The results of analysis for 1.5 bar internal pressure in the pipeline show that the von-Mises stress could be reduced as low as 20 MPa without larger pulling force refer to Fig. 5. The reason is that the increased internal overpressure would reduce the ovality of the HDPE pipeline. The resistance against buckling by applying an internal overpressure can increase the resistance to buckling more efficiently than the loss in resistance by reducing the pulling force from 80 ton to 50 ton. Curvature and bend radius are not affected as much as von-Mises stress.

The pulling force of 50 ton was maintained to give tension for controlling continuous sinking in the field. Two water pump was set in the barge to deliver water into the pipeline being charged with compressed air 1.5 bar.

4_CONCLUDING REMARKS

The HDPE pipeline in the marine environment has been providing various advantages such as immunity to galvanic corrosion, light weight, and flexibility. But sinking the HDPE pipeline safely into the seabed without failure requires rigorous installation analysis and sensitive control to prevent an abrupt change of pipeline. During the Djinet Combined Cycle Power Plant project in Algeria, a few lessons are learned. They are:

• The weighting of the pipeline is the most important factor to keep the pipeline with no movement against wave and current. The weighting block is generally constructed with concrete ranging of 25 to 50 % of the pipeline displacement. 40 % weighting block of the pipeline displacement was designed but reduced to 32 % considering trench effect.

• The lifting of the pipeline apart from appropriate distance in the inmost region could prevent the pipeline changing the shape abruptly at the moment of touching the bottom and making S-shape. Pipeline lifting of 60 ton in the 60m apart from the pipeline in most end was applied for the project.

• The pulling force to give tension into the pipeline will affect the bend radius and von-Mises stress in the pipeline during installation, specifically in the most area of the pipeline. Larger pulling force tends to make the pipeline experience lesser von-Mises stress. But internal overpressure could replace the larger pulling force with the smaller pulling force, which could lead to saving the charter fee for a barge with larger equipment for pulling force.

REFERENCES

1. AWWA. 2006. M55 PE pipe—design and installation. Denver, USA: American Water Works Association (AWWA).
2. Bergström, J.S. & Bischoff, J.E. 2010. An Advanced Thermomechanical Constitutive Model for UHMWPE. International Journal of Structural Changes in Solids 2(1): 31–39.
3. Bergström, J.S., Rimnac, C.M. and Kurtz, S.M. 2004. An augmented hybrid constitutive model for simulation of unloading and cyclic loading behavior of conventional and highly cross linked UHMWPE. Biomaterials 25 (11): 2171–2178.
4. Chen, Y., Davalos, J.F., Ray, I. & Kim, H. Y. 2007. Accelerated aging tests for evaluations of durability performance of FRP reinforcing bars for concrete structures. Composite Structures 78 (1): 101–111.
5. El-Sawy, K.M. 2001. Inelastic stability of tightly fitted cylindrical liners subjected to external uniform pressure. Thin-Walled Structures 39 (9): 731-744.
6. Glock, D. 1997. Behaviour of liners for rigid pipeline under external water pressure and thermal expansion. Der Stahlbau, 212-217.
7. Guermazi, N., Elleuch, K. & Ayedi, H.F. 2009. The effect of time and aging temperature on structural and mechanical properties of pipeline coating. Material and Design 30 (6): 2006-2010.
8. Ian Larsen. 2013. Design report for Ras Djinet seawater intake system
9. Idris, K. 2008. Calculation of concrete ballast requirement for subsea HDPE pipeline. Journal Infrastructure and Built Environment 4(2): 160-166.

10. Jacobsen, S. 1974. Buckling of circular rings and cylindrical tubes under external pressure. Water Power 26: 400-407.
11. Kang, J.S., Han, T.H., Kang, Y.J. & Yoo, C.H. 2009. Short-term and long-term behaviors of buried corrugated high-density polyethylene (HDPE) pipes. Composites Part B: Engineering 40 (5): 404-412.
12. Kim, Y. 2015. Installation and design of large diameter of HDPE pipeline for intake, The 10th Pipeline Technology Conference 2015, 8-10 June, Berlin, Germany.
13. Mohd Ishak, Z.A., Ishiaku, U.S. & Karger-Kocsis, J. 2000. Hygrothermal aging and fracture behavior of short-glass-fiber-reinforced rubber-toughened poly (butylenes terephthalate) composites. Composite Science and Technology 60 (6): 803–815.
14. Pegoretti, A. & Migliaresi, C. 2002. Effect of hydrothermal aging on the thermomechanical properties of a composite dental prosthetic material. Polymer Composites 23 (3): 342–351.
15. RPS. 2004. Rinker Pipeline Systems. New Orleans, LA, USA.
16. Rueda, F., Otegui, J.L. & Frontini, P.M. 2011. Numerical tool to model collapse of polymeric liners in pipelines. Engineering Failure Analysis 20: 25–34.
17. Rueda, F. Torres, J.P., Machado, M., Frontini, P.M. & Otegui, J.L. 2015. External pressure induced buckling collapse of high density polyethylene (HDPE) liners: FEM modeling and predictions. Thin-Walled Structures 96: 56-63.
18. Song, H.B., Kim, D.K., Choi, H.S. & Park, K.S. 2015. A study on structural stability of HDPE Pipe during installation, Journal of Korean Society for Advanced Composite Structures 6(1), 59-66.